J|A|C|S PERSPECTIVES

Published on Web 11/30/2009

New Light on Molecular and Materials Complexity: 4D Electron Imaging

Dmitry Shorokhov and Ahmed H. Zewail*

Physical Biology Center for Ultrafast Science and Technology, Arthur Amos Noyes Laboratory for Chemical Physics, California Institute of Technology, Pasadena, California 91125

Received September 2, 2009; E-mail: zewail@caltech.edu

Abstract: In this Perspective, 4D electron imaging is highlighted, after introducing some concepts, with an overview of selected applications that span chemical reactions, molecular interfaces, phase transitions, and nano(micro)mechanical systems. With the added dimension of time in microscopy, diffraction, and electron-energy-loss spectroscopy, the focus is on direct visualization of structural dynamics with atomic and nanoscale resolution in the four dimensions of space and time. This contribution provides an exposé of emerging developments and an outlook on future applications in materials and biological sciences.

1. Introduction

Of major impact in molecular and materials sciences is the ability to observe atoms at rest with angstrom-scale spatial resolution and atoms in motion with femtosecond-scale temporal resolution. X-ray and electron techniques have enabled structural determination, beginning with two-atom systems (crystals of sodium chloride or zinc sulfide) and now culminating in the determination of structures of molecular machines with the number of atoms exceeding 10^5. Similarly, for dynamics, the time scale at the beginning of the 20th century was practically seconds (hydrolysis of sugars); now, it has reached the atomic scale of femtoseconds and attoseconds.

For macromolecules, in the early days of DNA structural determination (1950s), a cardinal concept, in vogue at that time, was encapsulated in Francis Crick's statement: "If you want to know the function, determine the structure." This view pervaded the thinking at the time, and it was what drove Max Perutz and John Kendrew earlier in their studies of proteins. But as we learn more about complexity, it becomes clear that the so-called "structure−function" correlation is insufficient to establish the mechanisms that hold influence in complex systems. For example, the structures of many proteins have been determined, but we still do not understand how they fold, how they selectively recognize other molecules, and how the matrix water assists folding and molecular recognition. Similarly, for complex materials undergoing transformations such as phase transitions, chemical reactions, and crystallization, the pathways are multiple, and transient structures are numerous. Visualization of the changing structures during the course of functional operation is, therefore, of fundamental significance.

As particles with picometer wavelength, electrons can diffract with atomic-scale resolution, and they can be focused in a microscope. The power of electron diffraction and electron microscopy is manifested in the myriad of applications in different phases:[1] determination of (thousands of) molecular structures in the gase phase by L. Pauling and others; structural characterization of surfaces and materials by low-energy electron diffraction (LEED) and reflection high-energy electron diffraction (RHEED); and determination of 3D macromolecular structures (including membrane proteins). Though electron diffraction by thin liquid films was first explored by L. R. Maxwell as early as 1933, it was not until 1974 that suitable diffraction patterns of liquid water were obtained.[2] Since electrons strongly interact with air, electron scattering measurements are usually performed in vacuum, but new methods are providing the means for the studies of structures using environmental and cryo-microscopy. As outlined below, it is because of this strong interaction with matter that ultrashort electron pulses are capable of revealing transient structures of gases, molecular interfaces, and (thin) layers of materials.

Time-averaged structures are well suited to describe the equilibrium state of the system, but, in order to follow the dynamics of a transformation, the system must be brought to an initial nonequilibrium configuration. Earlier in the 1980s, with spectroscopic and mass spectrometric detection, the field of femtochemistry was developed to observe in real time transformations during the course of chemical reactions.[3] However, structural changes were only obtained for elementary systems.[4] For complex structures, a new approach was needed in order to visualize all motions at once. In this Perspective we highlight the principles and applications of 4D electron imaging, which has evolved into a field of study now embracing ultrafast electron diffraction (UED), crystallography (UEC), and microscopy (UEM). In what follows we discuss selected applications of the method in chemistry, materials science, and biology. With the added dimension of time,[5] and with the ever-increasing spatial and temporal resolution (currently, picometer and femtosecond, respectively), the focus is on direct visualization of structural dynamics in the four dimensions of space and time. Methods based on X-ray absorption and diffraction are not the subject of this Perspective.[6]

The outline is as follows. After a brief discussion of some key concepts, we provide examples in the study of complex isolated chemical reactions and interfaces, phase transitions of materials, macromolecular structures, and nanomechanical systems. We conclude with selected emerging developments and an outlook for future developments and applications.

10.1021/ja907432p

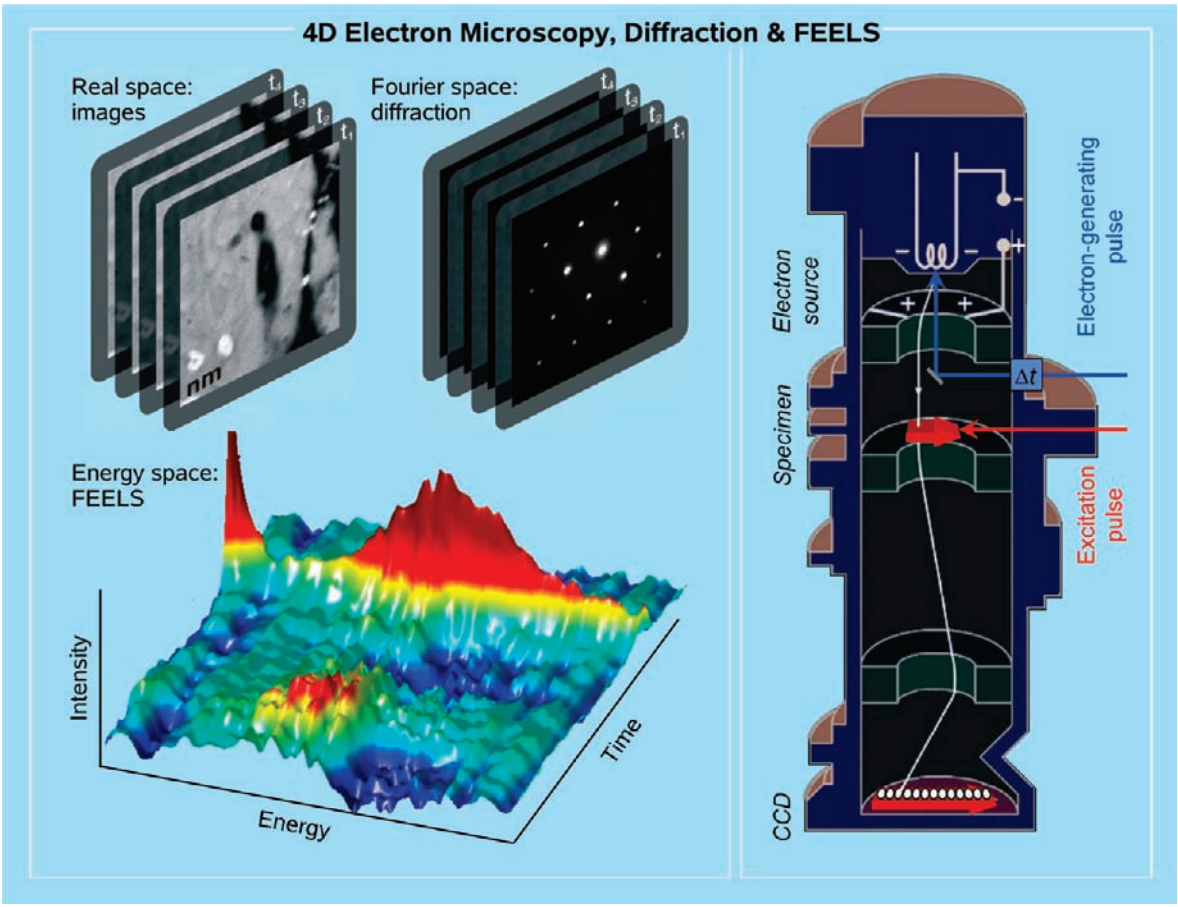

Figure 1. 4D electron imaging in real, Fourier, and energy spaces. Conceptual design of Caltech's UEM-2 is presented on the right; note the single-electron trajectory schematized in UEM. The atomic-scale (femtosecond) temporal resolution characteristic of the apparatus allows for direct visualization of physical, chemical, and biological processes in real time.

2. Some Principles of 4D Electron Imaging

In 4D electron imaging, as with stop-motion photography and flash stroboscopy,[7] the molecular motion has to be resolved into frames using a sequence of flashes, in our case the probing electron pulses. However, 4D electron imaging demands the marriage of ultrafast probing techniques with those of conventional microscopy and diffraction, as well as the development of concepts describing the simultaneous temporal and spatial resolutions of atomic scale. Of relevance here is the "*uncertainty relationship*" between time and energy and the apparent "uncertainty" that may limit the spatial resolution.[8,9] Since the first reports from this laboratory, the technical and theoretical machinery had to be further developed, and currently at Caltech there are five table-top instruments for studies of gases, condensed matter and biological systems.

The conceptual framework of the approach is as follows. Upon the initiation of the structural change (a physical, chemical, or biological process) either by heating of the sample or through electronic excitation induced by ultrashort laser pulses, a series of electron pulses is used to probe the specimen with a well-defined time delay. In this way we obtain electron diffraction patterns, microscopy images, and electron-energy-loss (EEL) spectra, all as a function of time. Such a series of images recorded at a number of delay times provides the temporal evolution of the structure, which can be recorded in the form of a movie. Isolated reactions are studied by using collisionless molecular beams (UED), while crystals and surfaces are examined in either the reflection or transmission mode (UEC). For microscopy, the electron beam typically penetrates a nanometer-scale sample (UEM). There is also another dimension to UEM, namely the *in situ* observation of nanoscale physical and mechanical phenomena (and biological imaging) with ultrashort electron pulses, as discussed below.

For real-space imaging—microscopy—the strict requirement for proper focusing was a real challenge. In order to reach the femtosecond domain, and possibly the attosecond domain of time resolution,[10] a new way of thinking was required. The paradigm shift was the realization that imaging can be achieved using timed and coherent single-electron packets,[1,9] which are free of space-charge effects. Images develop in about the same time as that of an *N*-electron pulse, but now the time resolution is under control. Increasing the number of electrons in the pulse can, in principle, result in a single-pulse ultrafast imaging,[11] especially suited for irreversible processes that result in permanent damage.

At 200 kV, the de Broglie wavelength of the UEM-2 microscope at Caltech (Figure 1)[12] is 2.5 pm. Unlike photons (bosons), each electron (fermion) occupies an exclusive volume of phase space according to the Pauli exclusion principle. It is important that the number of electrons in this space be very small in order to reach the single-electron imaging regime.[9] Given the speed of electrons and their dispersion, and the microscope divergence angle, it was shown that single-electron imaging can be achieved coherently with the volume being on the order of 10^6 nm^3. This is an important point for the atomic-scale studies of structural dynamics.[9] Figure 1 presents a layout

of UEM-2, displaying a single-electron trajectory in the microscope and the typical data obtained using different modes of operation: femtosecond-resolved electron-energy-loss spectra (FEELS); real-space image frames; and diffraction patterns. All of these can be obtained *in situ* in the microscope, as detailed below.

3. Applications

3.1. Structural Dynamics of Chemical Reactions. The simplest degree of structural change in complex systems would, superficially, seem to be that of chemical reactions involving a mere 10 or so atoms. However, such transformations result from many-body interactions, and, until recently, the determination of their *isolated* intermediate structures was impossible because of their fleeting nature, on the time scale of a picosecond or less. These transient structures are optically "dark" in that they undergo radiationless transitions into reactive or nonreactive channels, and in most cases they do not emit light. The bifurcation obscures the mechanism, and only through studies of both their structures and dynamics[13] can one resolve the complexity of pathways and elucidate mechanisms—with this understanding it is hoped that the system behavior could be controlled. It is important to realize that even for a system of three atoms, trajectories of motion can result in different final structures of several channels: an ABC system is, in principle, destined to produce AB + C, A + BC, AC + B, and A + B + C.

With a properly chosen frame-referencing, i.e., with an adequate selection of the two points in time that correspond to the two different states of the system under study, typically before ($t < 0$) and after ($t > 0$) the arrival of the exciting laser pulse, or two points on the positive time axis, the spatiotemporal evolution of transient structures has now been extensively explored for different chemical processes. A classic example is the transient behavior observed upon consecutive elimination of iodine from 1,2-diiodotetrafluoroethane ($C_2F_4I_2$) to form tetrafluoroethylene (C_2F_4) on the ultrafast time scale[13] and the determination of the structure of the picosecond-lived C_2F_4I intermediate (Figure 2).

In order to resolve structural changes during the course of the elimination reaction, the diffraction pattern of the *anti*−*gauche* conformation mixture characteristic of the ground state of $C_2F_4I_2$ at $t = -95$ ps (Figure 2b) was referenced to those obtained for a variety of time points corresponding to $t > 0$, and the resulting *diffraction differences* were analyzed. The significance of this referencing is evident in the results of Figure 2e,f; a reference at positive time shows the absence of I··I nonbonded distance, as the first C−I bond breaks on the sub-picosecond time scale. The results of least-squares structure refinements supported the nonconcerted nature of the reaction: the first step ($C_2F_4I_2 \rightarrow C_2F_4I + I$) is essentially complete within 5 ps (see evolution in Figure 2), whereas the second step ($C_2F_4I \rightarrow C_2F_4 + I$) takes place with a time constant of 26 ± 7 ps. The structure of the intermediate was determined using the difference curves. The first step is dissociative and occurs in ~200 fs, whereas the second step is a barrier-crossing process involving energy redistribution.[14,15]

Knowing the time scales involved, two structures were considered for C_2F_4I: a *classical* structure, in which the primary halide (I) resides predominantly on one $-CF_2$ moiety, and a *bridged* structure, in which the primary halide is shared equally between the two $-CF_2$ moieties (Figure 2c,d). To explore detailed structural features of the radical, the diffraction difference curves were fit separately with either the bridged radical structure or the classical *anti* and *gauche* radical structures obtained using *ab initio* calculations.[15] Theoretical curves for the classical structures provide a very good fit to the experimental data, whereas the fit to the bridged structure is poor (Figure 2c,d), thereby elucidating the nature of the intermediate: the structure of the C_2F_4I radical is classical.

The evolution of the reaction reflects changes in bond distances and angles. The C−I and C−C distances of the intermediate [2.153(13) and 1.48(5) Å] are, respectively, longer and shorter than those of the reactant [2.136(7) and 1.534(13) Å]. These results elucidate the increased C−C and decreased C−I bond order resulting from the formation of the transient C_2F_4I structure. Moreover, the C−C−F′ and F′−C−F′ angles (Figure 2a) become larger than the corresponding angles of the reactant (by ~9° and ~12°, respectively), suggesting that the intermediate relaxes following the loss of the first I atom. These structural dynamics provide the understanding for the retention of stereochemistry in this class of reactions. One important conclusion is that the retention of stereochemistry is dynamical in origin (not electronic structural changes), in that the bonds break before rotations scramble the orientation. Recently, the same class of reactions was studied in liquid methanol by Ihee and co-workers using X-ray scattering (XRS). The transient structure of CF_2CF_2I was also found to be classical,[13d] but the secondary dissociation slows down by a factor of 6 in methanol because of the solvent influence. The presence of solvent could lead to faster energy redistribution, change in reaction barrier height, and/or caging of fragments. Interestingly, the authors found a different intermediate in the case of ICH_2CH_2I.[13e,f]

With the same methodology, other reactions and intermediate structures involved in radiationless processes have also been studied. In Figure 3, some of the results obtained for the ring-opening (or lack thereof) in pyridines are shown to display the large change in bonding—including disappearance of old bonds in the case of pyridine—as a function of time. A summary of these and other recently studied structures is given in Scheme 1 (references to the original work are given in the footnote).

3.2. Molecular Interfaces. Interfacial assemblies of nanometer scale are challenging to determine, yet their structures and dynamics are of utmost importance. Perhaps water and ice are the supreme examples. With UEC, the problem of interfacial water was addressed by determining both the structure and dynamics using hydrophobic or hydrophilic surface substrates.[16] The interfacial and ordered (crystalline) structure was evident from the Bragg diffraction, and the layered and disordered (polycrystalline) structure was identified from the Debye−Scherrer rings (Figure 4a). The temporal evolution of interfacial water and layered ice after the temperature jump to the substrate was studied with monolayer sensitivity.

On the hydrophilic surface substrate (chlorine-terminated silicon), the structure was found to be cubic (I_c), not hexagonal (I_h); on the hydrophobic surface (hydrogen-terminated silicon), the structure was still cubic, but very different in the degree of order. As detailed elsewhere,[16a] the structural dynamics are distinctively different for the two phases. The interface is dominated by polycrystalline I_c, but coexisting in this phase are crystallite structures not adjacent to the surface of the substrate. The change in the structure of I_c has different temporal behaviors reflecting differences in the transfer of energy to polycrystalline and crystallite I_c. The issues of interest are the coexistence of these structures, their different dynamics, and the time scales for energy transfer and disruption of the hydrogen bond network.

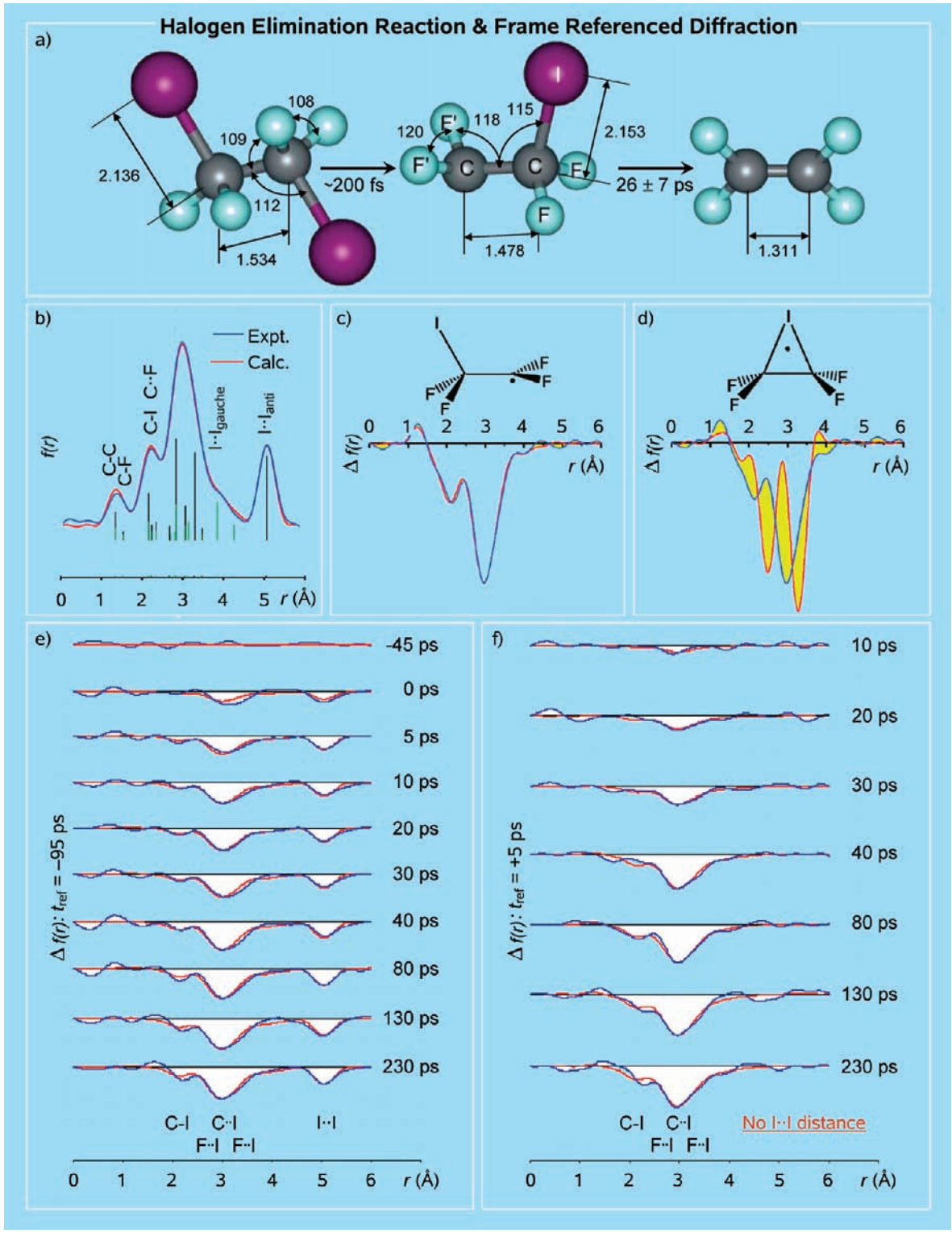

Figure 2. Structural dynamics of the elimination reaction of $C_2F_4I_2$. Reactant, intermediate, and product structures were determined under collisionless condition (a). Shown are UED patterns of the *anti*−*gauche* conformation mixture characteristic of the reactant as obtained for the ground state (b); internuclear distances for the *anti* (black) and *gauche* (green) isomers are indicated by vertical bars at the bottom of the panel. The structure of the intermediate is determined to be classical (c), not bridged (d), as evidenced by the agreement between diffraction theory and experiment; the discrepancy between theory and experiment is indicated in yellow (c,d). Frame-referencing reveals temporal changes in diffraction with respect to the two different reference points, before (e) and after (f) the arrival of the exciting laser pulse. Note the absence of the I··I peak in (f).[13a]

At the microscopic level, several conclusions were drawn. First, the reaction coordinate for breaking hydrogen bonds involves a significant contribution from the O··O distances. This is evidenced in the depletion with time of the corresponding peak in the radial distribution function. Second, the time scale of energy dissipation in the layered structure must be faster than that of desorption, as no loss of water molecules was observed. Third, the time scale of the dynamics at the interface is similar to that of water at protein surfaces. Finally, the order of water molecules at the interface is of high degree. Using molecular

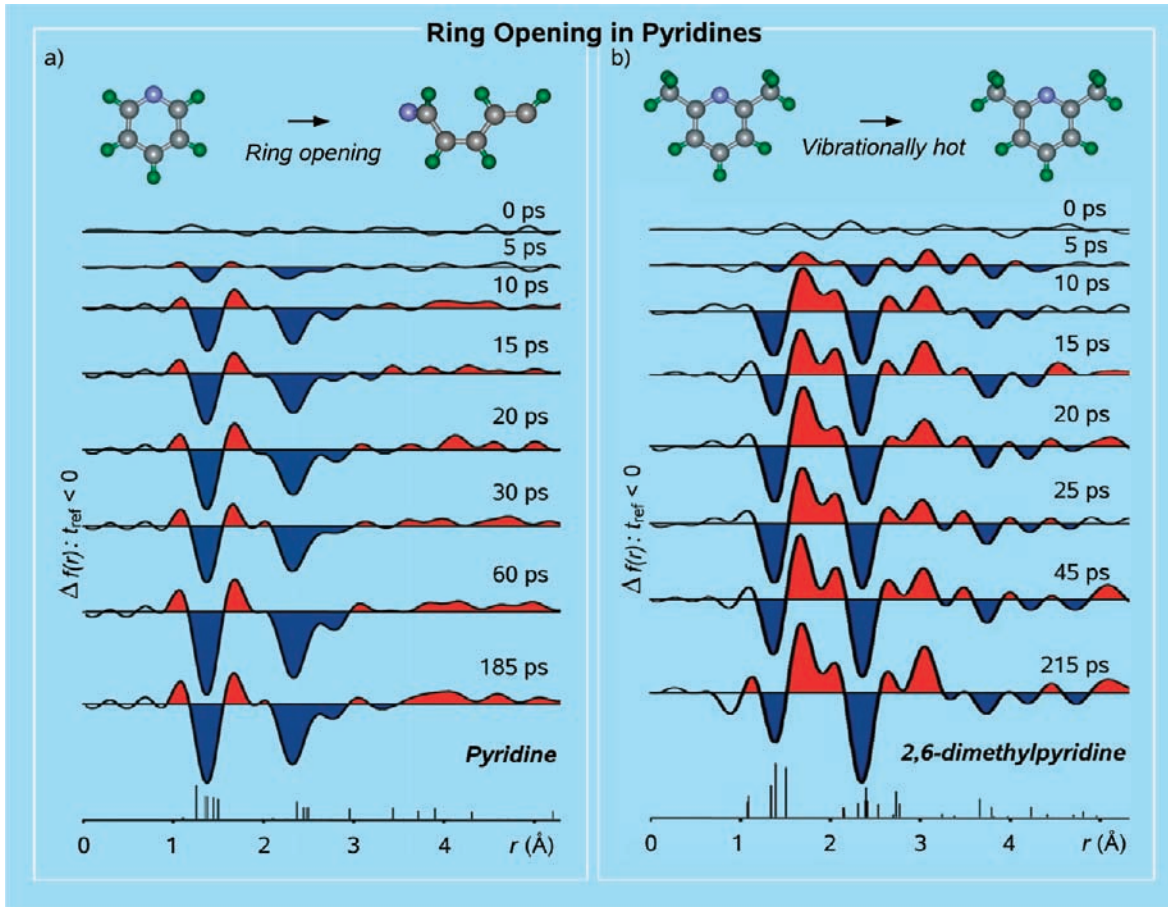

Figure 3. Ring-opening in pyridines as studied by UED. Shown is the temporal evolution of radial distribution functions for pyridine (a) and 2,6-dimethylpyridine (b). The negative (blue) regions of diffraction difference curves with reference to negative times represent the loss of "old" interatomic distances; the positive (red) regions of the curves correspond to gain of "new" interatomic distances. Note that unlike pyridine, which undergoes a ring-opening reaction, 2,6-dimethylpyridine yields vibrationally hot ground-state structures upon photoexcitation.[13b]

dynamics (MD) simulations, the nature of forces (the atomic-scale description) and the degree of ordering were examined in collaboration with Parrinello's group, elucidating features of crystallization, amorphization, and the time scales involved.[17]

For water on graphite (Figure 4b),[16b] one of the unexpected observations made was a structural isosbestic point, similar to the one found in the study of cuprates (see below). In the case of the ice−graphite composite, however, the surface structure plays a crucial role. The lattice of graphite has been shown to undergo a contraction followed by a large expansion along the *c*-axis with a time constant of ∼7 ps.[18] For water on graphite, the "old-structure" disappearance time observed (∼10 ps) matches well with the 7-ps time scale, indicating that excitation of the original assembly is due to the vibrational coupling of ice with underlying graphite. In other words, the ice film receives the vibrational energy from graphite and undergoes ultrafast softening ("melting"), which causes the diffraction intensity to decrease by ∼20%. To accommodate such large-amplitude structural perturbation and the undulating substrate, the stack of (111) water bilayers expands in a phase transformation, with a rise time of ∼20 ps. Later on, when the vibrational motion of graphite comes to an end, the interfacial assembly is able to form an even better conformation (structural annealing) that enhances the diffraction intensity. When this stage is reached, the transformed ice structure behaves collectively and begins its recovery as a single unit, which occurs with two time constants of 75(5) and 390(35) ps. The overall restructuring can be reproduced theoretically using equations of heat diffusion to the substrate. Accordingly, there is no bottleneck in the energy exchange between water and graphite, neither in cooling nor in the initial expansion of the water assembly. The transformations span the picosecond to nanosecond time scales (Figure 4).

In comparing the behavior on graphite with that on another hydrophobic surface, the hydrogen-terminated Si (111), it is concluded that potential energy interactions (simple bonding energetics) of water−water and water−substrate are insufficient to describe the relatively high degree of water ordering observed on graphite. Substrate morphology at interfaces is as important as binary bonding energies in confining the structure on the nanometer scale. For ice on Pt (111), both the surface steps and screw dislocations are critical in the formation of metastable cubic structure (and not the hexagonal one) and in the growth. Spectroscopic investigation[19] of interfacial (D_2O) ice, using sum-frequency generation with longer time resolution, suggested the presence of melted regions, but neither the structure nor the order was possible to observe with atomic-scale resolutions. Unlike in conventional heating, the lack of sublimation of water on the time scale of observed dynamics is due to ultrafast melting and energy exchange in the water assembly; see Figure 4.[16b]

3.3. Bilayers, Phospholipids, and Cells. The simplest of membrane-type structures is perhaps a bilayer of fatty acids. These long hydrocarbon chains self-assemble on surfaces (substrates) and can also be made as "2D crystals". To achieve

Scheme 1. Molecular Structures and Dynamical Processes Studied Recently by UED[a]

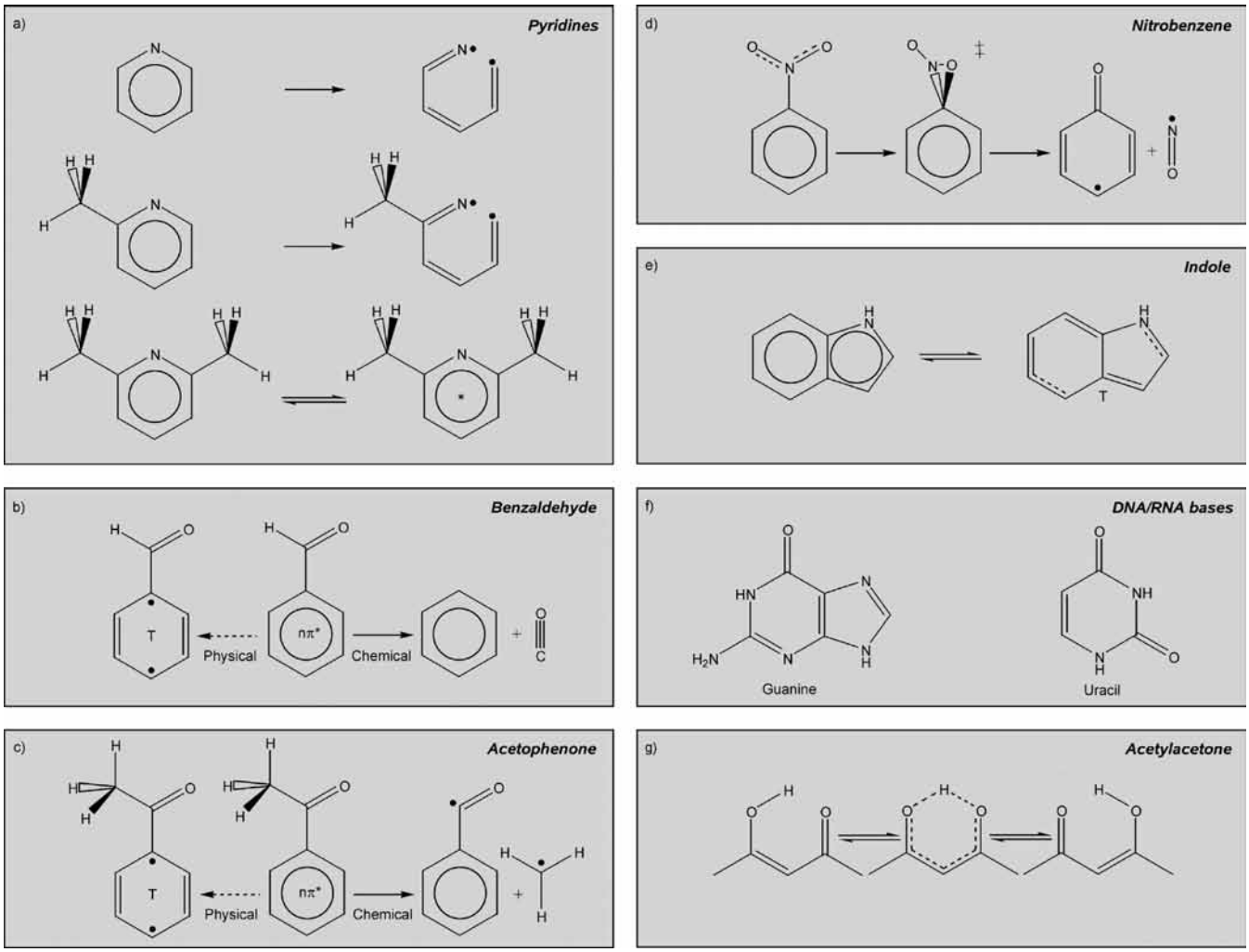

[a] Shown are ring-opening reactions in pyridine and 2-methylpyridine, as well as the lack thereof in 2,6-dimethylpyridine (a);[13b] photophysical ($n\pi^*$ to triplet-state diradical structure conversion) and photochemical (decomposition) processes in benzaldehyde (b) and acetophenone (c);[46] NO-group release from nitrobenzene (d);[47] optically dark triplet-state structure of the biological chromophore indole (e);[48] molecular structures of DNA/RNA bases, guanine and uracil, as obtained using a novel laser desorption technique (f);[49] and hydrogen atom transfer in acetylacetone (g).[50] A comprehensive review of earlier UED work is provided in ref 13c.

crystallinity, the methodology of Langmuir−Blodgett (LB) films is invoked, providing control over pH, thickness, and pressure. In these studies,[20] the *T*-jump of the substrate, or the expansion force of surface atoms, is exploited to heat the adsorbed layers deposited on either a hydrophobic or hydrophilic substrate. The femtosecond infrared pulse has no resonance for absorption to the adsorbate. The studies made for monolayers, bilayers, and multilayers of fatty acids and phospholipids provide an opportunity to determine structural dynamics and to examine nanoscale changes due to the transition from two to three dimensions.

Four types of UEC measurements have been made: the change of position of Bragg spots with time, the temporal evolution of the diffraction intensity, the increase/decrease in diffraction spot width, and the change of diffraction with the angle of incidence (rocking curve) and azimuthal angle for the position of the electron pulse relative to the zone axis of the substrate. The static, time-averaged crystal structures of the adsorbates were established by determining the orientation of the chains relative to surface plane and by measuring the $-CH_2-CH_2-CH_2-$ chain distances, which define the sub-unit-cell dimensions (Figure 5). For arachidic fatty acid, depending on pH and deposition conditions, a_0 ranges from 4.7 to 4.9 Å, b_0 ranges from 8.0 to 8.9 Å, and c_0 ranges from 2.54 to 2.59 Å. For dimyristoyl phosphatidic acid (DMPA), $c_0 = 2.54$ Å.

The net change in displacement is determined by the impulsive force of the substrate (including coupling to adsorbate), and the maximum value of the extension depends on elasticity and heat capacity. If heating occurs in an equilibrated system, the change in the value of c_0 with temperature, Δc_0, should be independent of the number of $-CH_2-CH_2-CH_2-$ subunits in the chain; because of anharmonicity, $\Delta c_0/c_0$ is simply given by α, the thermal expansion coefficient, which is typically very small, $\Delta c_0/c_0 \approx 10^{-5}$ K^{-1}. For a 10-degree rise, this expansion would be on the order of 10^{-4} Å, whereas the observed transient change is as large as 0.01 Å.

In the nonequilibrium regime, the large amplitude of expansion is understood, when considering chain dynamics, even for a harmonic system.[21] The impulsive force at short times induces a large change in the value of Δc_0 as the disturbance (wave-type) accumulates to give the net effect that is dependent on the number of C atoms. In other words, as the disturbance passes

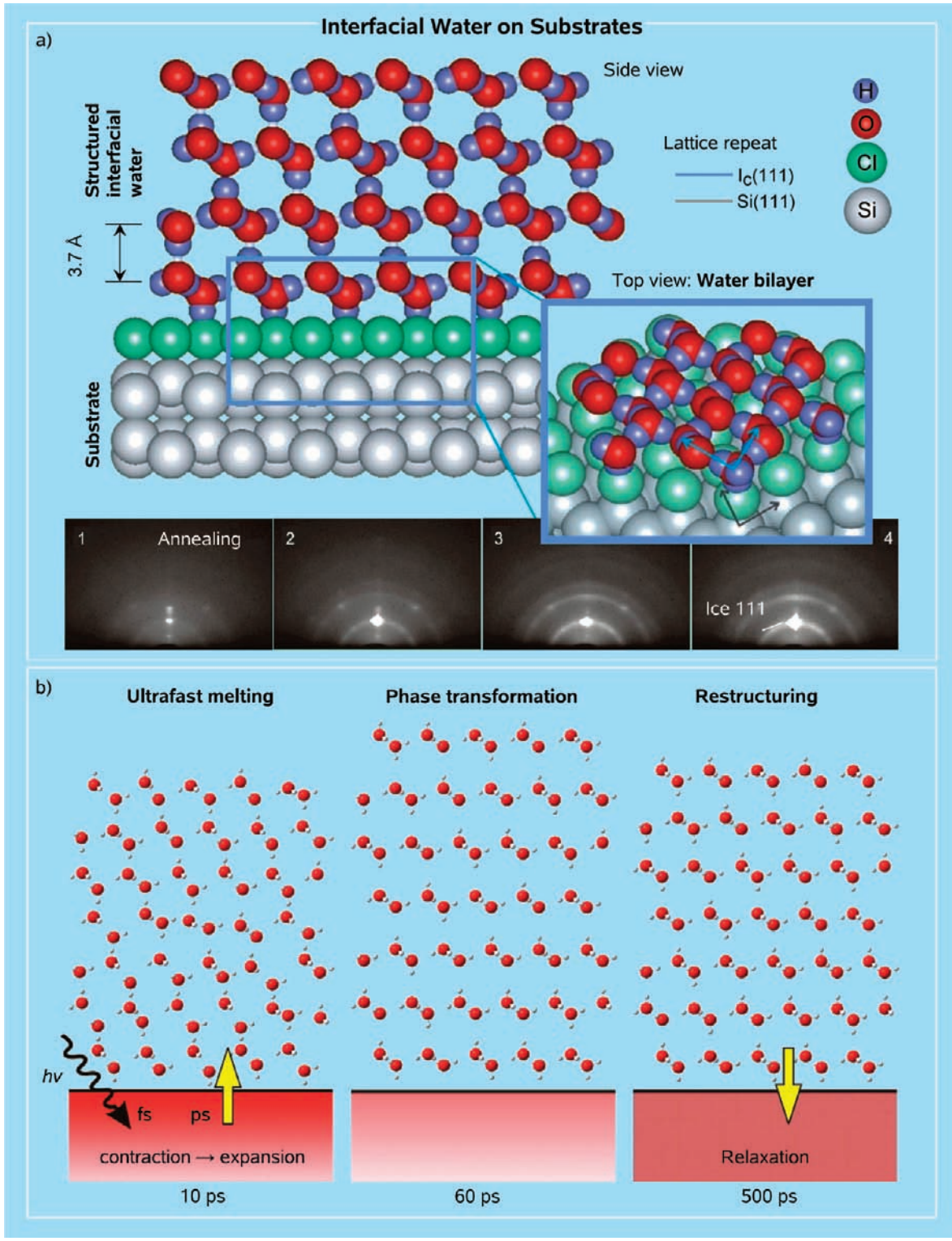

Figure 4. Structural dynamics of interfacial water as studied by UEC. The chlorine termination on a Si(111) substrate forms a hydrophilic layer that orients the water bilayer. The ordered stacking persists for three to four bilayers (~1 nm) before disorientation takes place and results in crystallite islands, forming the layered structure. Note the coexistence of two phases, as evidenced by Bragg spots and Debye−Scherrer rings (a). Also shown is the schematic representation of the dynamics for the ice layers on graphite (b). Yellow arrows denote the direction of energy transfer. Similarly to superconducting cuprates, the formation of the expanded ice phase involves the structural isosbestic point at a well-defined value of *s* (see text and Figure 7b).[16]

through the bonds, the diffraction amplitude builds up and exhibits a delay, ultimately giving rise to a large total amplitude for the change. This picture also explains the dependence of expansion on the total length of the chains, the increase in the initial maximum amplitude as the temperature of the substrate increases, and the effect of strong (hydrophilic) vs weak (hydrophobic) binding to the substrate. Quantification of the total change must take into account the form of the substrate

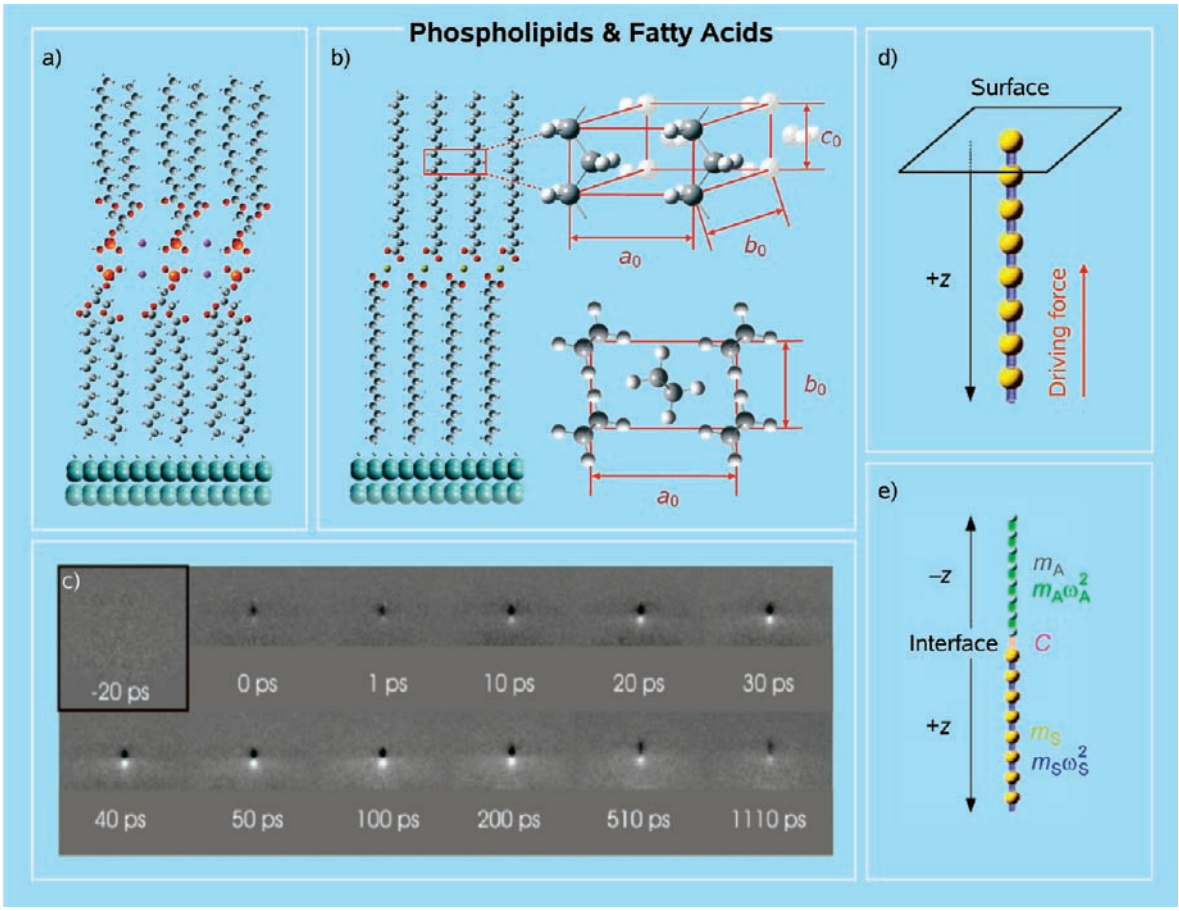

Figure 5. UEC of 2D phospholipid and fatty-acid bilayers. Shown are the substrate−adsorbate structures determined (a,b) and the dynamics obtained (c) for arachidic (eicosanoic) acid assembly by frame-referencing, following the heat pulse transfer to the substrate. The frames at 0 and 1 ps show the onset of structural changes, and the frames at longer times display the restructuring toward the equilibrium state.[20] Also shown are the 1D atomic chains which represent substrate-only (d) and substrate−adsorbate (e) lattices used in the theoretical model.[21a]

force and variation in the density of the LB films upon going from single to multiple layers, as well as the (zone-axis) morphology change.

Considering the fact that the initial change in intensity (and elongation) occurs on the 10-ps time scale and that the distance traveled is approximately 20 Å (for a monolayer), the speed of propagation should be sub-kilometers per second, which is reaching that of the propagation of sound waves. Because the substrate is heated through optical and acoustic phonons, the rise is convoluted with the process of phonon generation, which is on the time scale of 10 ps. Accordingly, the speed could be of a higher value, reflecting the actual speed of sound in the layers. Future experiments will further investigate this region in order to elucidate the maximum extension possible and the expected features of coherent motion. The model of coherent coupling among bonds in the underdamped regime of harmonic motions yields results vastly different from those of the diffusive behavior in the overdamped regime, but it has some common characteristics to the well-known Fermi-Pasta-Ulam model of anharmonically coupled chain dynamics,[21] and to a recent optical study of thermal conductance of molecular chains.[22] Self-assembled systems exhibit more diffuse scattering, but at shorter times some order was revealed.[23]

UEM, with real-space imaging and with diffraction, has the potential of providing biological structures of complexes and conformations. The regularity of pulsed dosing is unique for the control of time and, perhaps, energy redistribution and heat dissipation. The pulsed characteristic may lead to a better resolution of single-particle imaging and, just as importantly, will provide the time scale of structural change, as discussed toward the end of this Perspective. The first effort in this regard was directed toward the imaging of a stained cell with UEM-1.[24] For such a proof of principle of real-space imaging, the issues involved were the extent of lateral coherence and sensitivity to contrast imaging. Images (UEM-1) for cells derived from the small intestines of a 4-day-old rat were recorded. The specimen was prepared using standard thin-section methods. The cells were positively stained with uranyl acetate, causing them to appear dark on a bright background.

Figure 6 shows the UEM images of the cells at two different magnifications. The images were obtained using ultrashort pulses of UEM with exposure times of a few seconds; such exposure times compare well with those of standard EM imaging. In the figure, both the microvilli and the subcellular vesicles of the epithelial cells can be visualized. More recently, in UEM-2, it was possible to obtain *phase-contrast* images of bacterial cells in vitreous water (cryo-microscopy) showing the membrane structure and flagellum of the cell, as displayed in Figure 6. In the same figure, the results of phase-contrast imaging of a crystal of catalase protein are shown to display the resolution of the crystal-plane separation (9.3 nm). We will address the opportunities and challenges of bio-UEM imaging in section 4.

3.4. Structural Phase Transitions and Crystallization. Because of the combined microscopy−diffraction capabilities of

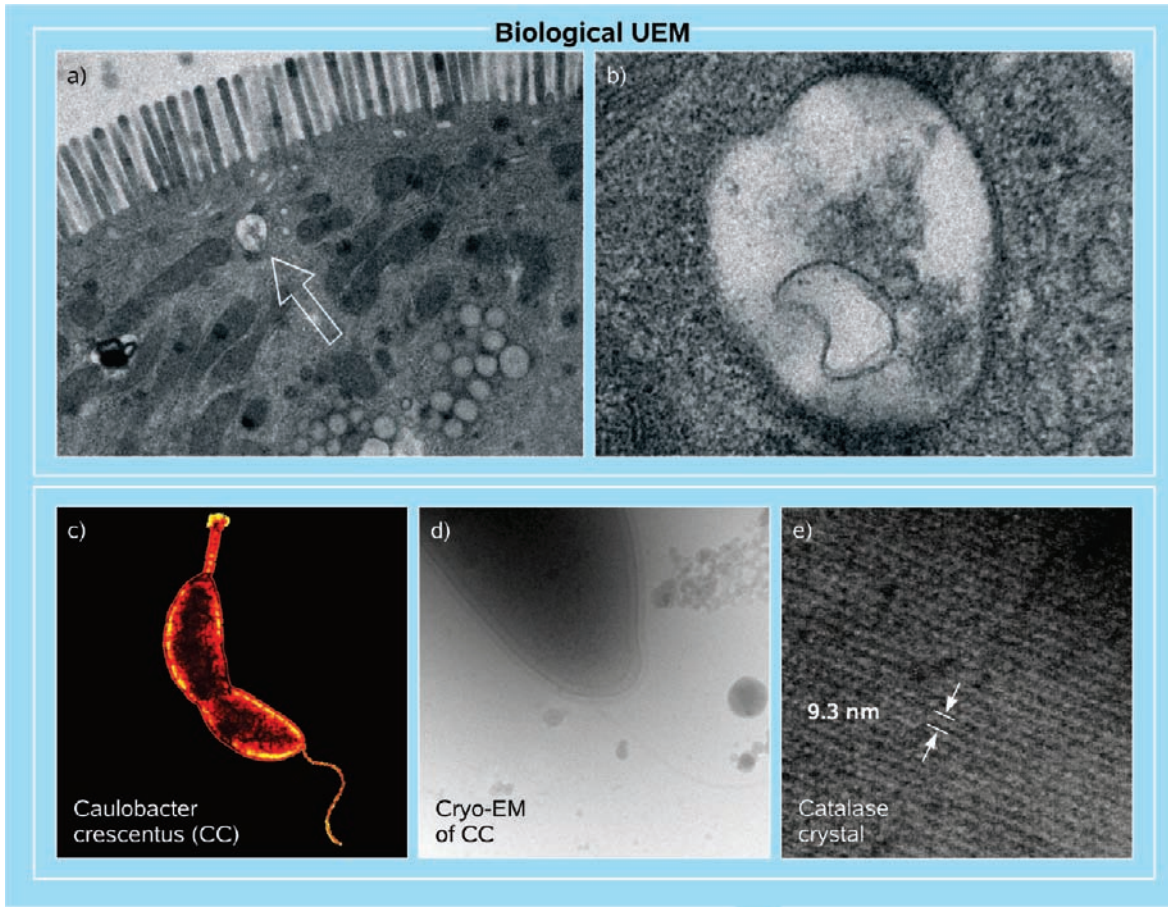

Figure 6. Biological UEM. Shown are images of positively stained rat intestinal cells (a,b). The images reveal the microvilli in the intestinal epithelium of the neonatal rat along with numerous small vesicles throughout the cytoplasm. The arrow on the left indicates the vesicle magnified on the right.[24] Also presented are bacterial cell (*Caulobacter crescentus,* CC; adapted from MicrobeWiki) and a high-resolution image of CC as obtained using cryo-UEM in vitreous ice, showing membrane structure and flagellum (c,d). A high-resolution image of the catalase protein crystal showing the planes with interplane separation of 9.3 nm is displayed in panel (e).[9]

UEC and UEM, they provide unique dimensions in the study of phase transitions, quantum wells, and novel materials of nanometer-length scale. Three examples are given here for studies of the temperature-induced structural (metal−insulator) transition in vanadium dioxide, the transient structures of superconducting cuprates, and nucleation in the crystallization process of amorphous silicon.

3.4.1. Metal−Insulator Phase Transitions. These transitions are known to be abundant in many systems.[25] UEM imaging of films of VO_2 reveals clearly the occurrence of the phase transition in crystallites of the nanometer scale.[26,27] Both the ultrafast insulator-to-metal transition and the slower recovery were observed, and theoretical considerations of the effects of connectivity and diffusion account for the observed behavior.[26,27] The UEC study was performed both on films and on single crystals of VO_2. The phase transition exhibits a well-defined hysteresis between the two thermodynamically stable structures (Figure 7a). In order to map pathways of motion, all observed Bragg diffractions of different planes and zone axes were examined on the femtosecond-to-nanosecond time scale.[28] Because the transformation takes place in a strongly correlated system, the dependence on excitation fluence is evident in a threshold behavior, and such dependence has been studied at short and long times to elucidate the nonequilibrium transition from local atomic motions to shear at sound wave (and carrier) velocity.

As discussed above for chemical reactions, the concept of concerted (or concurrent) vs consecutive nuclear motions, which deal with reorganization of the lattice and microscopic restructuring within unit cells, becomes important to understanding the elementary steps of the mechanism. The 3D sampling of diffraction and long-range order studied allow for the separation of different nuclear motions, which are mirrored in the temporal change of the structure factor for various Miller indices. For two different kinds of investigated Bragg spots (*hkl*), characterized by $h \neq 0$ and $h = 0$, two different types of dynamics were observed: a femtosecond process (∼300 fs) and another process with a time constant reaching 10 ps. This distinct behavior in dynamics indicates stepwise atomic motions along different directions. Because an atomic movement along a certain direction can only affect such Bragg spots that have nonzero contributions in the corresponding Miller indices, it was concluded that the initial femtosecond motion is along the *a*-axis (Figure 7a), which is the direction of the V−V bond in the monoclinic structure.

From a chemical perspective, the excitation is to an antibonding state, which instantly results in a repulsive force on the atoms, and they separate along the bond direction. In sequence and on a slower time scale, the unit cell transforms toward the configuration of the metallic, rutile phase. On the nanosecond time scale, the system reaches equilibration

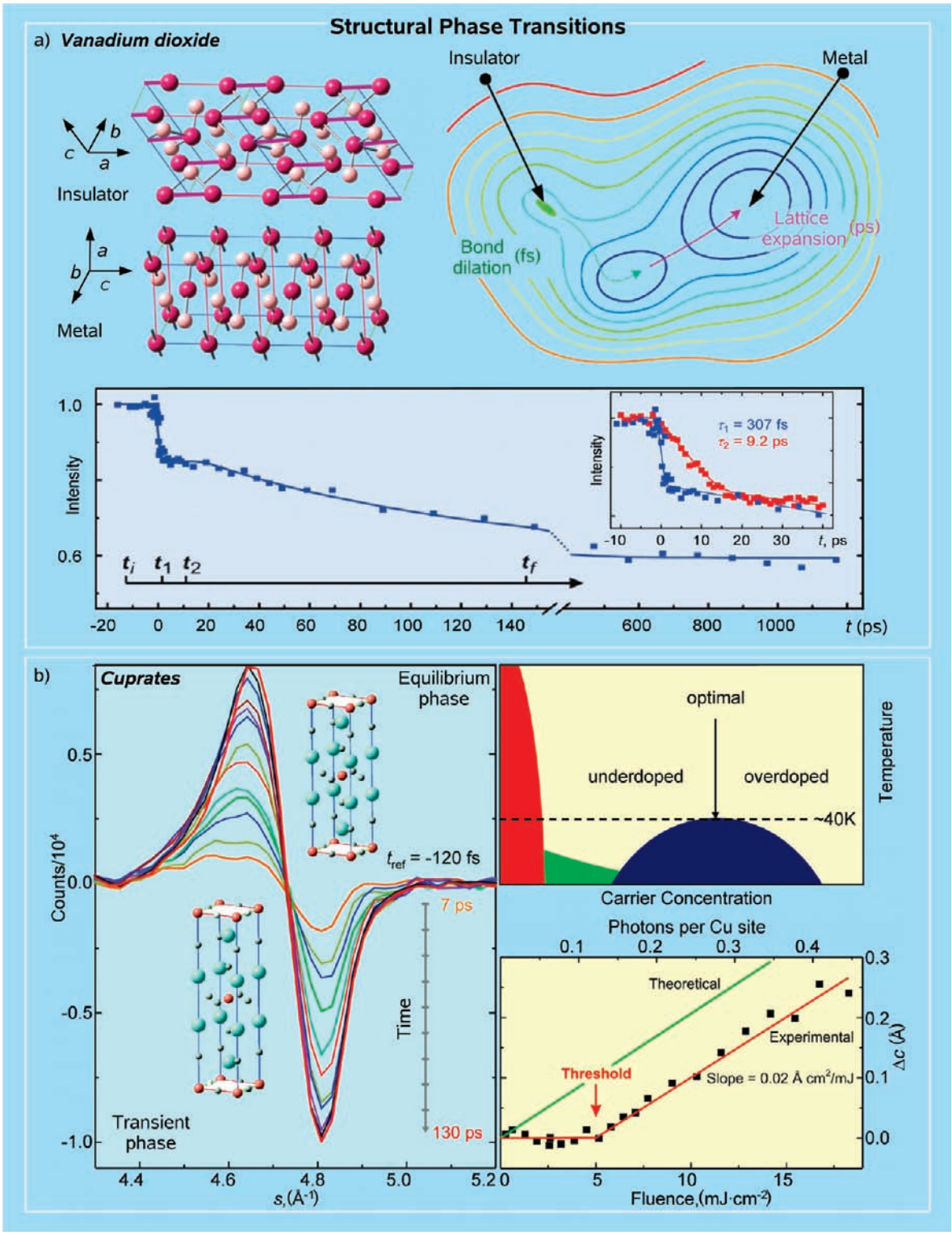

Figure 7. Ultrafast dynamics of structural phase transitions. Bragg diffractions of different directions and zone axes, when temporally resolved, indicate that the insulator-to-metal transition between the monoclinic and tetragonal structures of vanadium dioxide (upper left) occurs stepwise on the femtosecond and picosecond time scales, as depicted in the two-coordinate energy landscape (upper right). The full temporal behavior is illustrated at the bottom (a).[28] Also shown is a structural phase transition in oxygen-doped cuprate, $La_2CuO_{4+\delta}$ (b). Dispalyed are the schematic phase diagram (upper right) and the fluence dependence of the structural change (lower right) for $La_2CuO_{4+\delta}$. The temporal evolution of the referenced diffraction profile (left) indicates the depletion of the initial structure and the buildup of the transient-phase structure. Note the presence of the *isosbestic point* at ~4.76 $Å^{-1}$ and the threshold at ~5 mJ/cm^2, which corresponds to a critical value for the number of photons (0.12) per copper site.[29]

nearly at sound wave shear motion. These observations of stepwise atomic motions indicate that the phase transition proceeds by a nondirect pathway on the multidimensional potential energy surface and not by a direct structural conversion, thus defining a transition-state intermediate for the metal-to-insulator transition (see Figure 7a).

3.4.2. Superconducting Cuprates. The second example for nonequilibrium structural phase transitions is that of superconducting cuprates.[29,30] The specific material studied is oxygen-doped $La_2CuO_{4+\delta}$ (LCO); the undoped material is an antiferromagnetic Mott insulator, whereas doping confers superconductivity below 32 K and metallic properties at room temperature. From the observed Bragg spots, the unit-cell parameters were obtained using the patterns for different zone axes: $a = b = 3.8(1)$, $c = 13.1(1)$ Å. Structural dynamics were then obtained by recording the diffraction frames at different times, before and after the arrival of the optical excitation pulse. What was expected, as observed in previous UEC studies in this laboratory, is that the peak shifts continuously and the intensity decreases with time. Instead, all curves obtained at different times cross at a single value of *s*-coordinate, which parametrizes the momentum-transfer space. This intensity sharing with a common crossing point, a structural *isosbestic point*, indicates a transition from the initial phase to a new (transient) phase.

The structural interconversion displaying the isosbestic point is illustrated in Figure 7b. The diffraction difference profile, as a function of time, reveals the depletion of initial structure and the accumulation of the transient-phase structure. The population of the initial (transient) phase decays (builds up) with a time constant of 27 ps, but the formed phase restructures on a much longer time scale (307 ps). Because the linear expansion coefficient is $\alpha_l \leq 1.0 \times 10^{-5}$ K^{-1}, the observed 2.5% increase in the lattice constant would correspond to an unphysical 2500 K rise in the lattice temperature at equilibrium. Another striking feature of this structural phase transition is its dependence on the fluence of the initiating pulse. A threshold was observed, above which the lattice constant of the transient-phase structure changes linearly with the fluence (Figure 7b).

The transformation at 1.55 eV is the result of a charge transfer from oxygen (O^{2-}) to copper (Cu^{2+}) in the $a-b$ copper−oxygen planes, as reported in the literature. With the lattice relaxation being involved, the excitation is shared microscopically (exciton type), and finally a transition to a transient phase is made (macroscopic domain). The net charge distribution in the transient phase results in the weakening of interplanar Coulomb attractions, leading to expansion along the *c*-axis. The behavior is nonlinear in that, when the number of transformed sites is below a critical value, the macroscopic transition is not sustainable. The crystal domain is greater than 20 nm^2, and symmetry breaking is not evident because charge transfer is in a plane perpendicular to the *c*-axis expansion. By consideration of Madelung energy and charge distributions, the linear dependence on fluence and the large values of expansion were accounted for.

The transient-phase structures, which are inaccessible by means of equilibrium methods, are undetectable by optical probes with wavelengths longer than lattice spacings. Moreover, the time scales of optical response and structural changes are very different. For the cuprate studied, the observed phase transition is the result of electronic charge redistribution and lattice collective interactions to form domains. The similarity of the apparent threshold for "photon doping" at ~0.12 photons per copper site and the "chemical doping" at fractional charge of 0.16 per copper site, required for superconductivity, may have its origin in the nature of the photoinduced inverse Mott transition. If general, the implications are significant.

More recently, these studies have been extended to other cuprates of different structures, and for various doping levels. In these studies,[30a] the polarization of the exciting pulse was exploited in order to elucidate the mechanism. It was concluded, at least in these systems, that the electron−phonon coupling is a significant player in structural changes and in electron correlation. Such a condition is at the heart of the mechanism for high T_c materials—phonons vs magnetic interactions.[30]

3.4.3. Nucleation and Crystallization. The final example given here is that of nucleation and crystallization. The transformation of amorphous structures, such as liquids or random-coiled proteins, into ordered structures involves complex dynamical processes that ultimately lead to the final native state. The mechanism is determined by the scales of time, length, and energy as they define the nature of the elementary steps involved. To observe nonequilibrium irreversible transformations on the time-length scale of the phenomena, the UEM-2 apparatus was operated in the single-pulse mode. Using this mode of imaging, it was possible to visualize the irreversible processes of melting and crystallization in silicon,[31] a complex transition involving nucleation and growth on the nanosecond-to-microsecond time scale. Earlier, surface melting was observed on the picosecond time scale in one of the first UEC studies from this laboratory (see below).

To initiate crystallization from the amorphous phase, a single optical pulse at a fixed energy was used, while a single pulse of electrons imaged selectively in space the transformation as the structure was continuously changing with time. With selected-area diffraction, the amorphous and crystalline phases were identified, and the temporal profile of (structural) crystallization in the embryonic stages was obtained for the entire image. Amorphous nanoscale surface melting is ultrafast within 10 ps,[32] but crystallization takes place on a significantly longer time scale(s). On the nanosecond time scale, there is no significant heat diffusion within the probed volume, and two main processes were identified: a *coherent* nanoscale layer propagation at ~15 m/s (explosive growth) and another that occurs with much slower velocity. Both the nanosecond and femtosecond pulses of UEM were used in this study, and below we discuss the significance in the description of the dynamics observed *in situ* as the transformation unfolds. Figure 8 depicts the different zones identified in diffraction and imaging.

A simple model of explosive crystallization starting at the edge of zone *C* at $t = 0$ and traveling at 15 m/s across zone *c* yields a duration of 1.2 μs for contributions to the total signal from zone *c* alone (see Figure 8a). Taking a propagation time of ~0.4 μs gives a distance in zone *c* of ~6 μm and a 2D area accounting for ~20% of the final signal, which is consistent with the explosive wave being effective to nearly half of the measured value at that time. The step was observed in the kinetic profile, which appears to be from a delayed process, and was attributed to the super-lateral growth that is of a slower nature. Thus, from the evolution of crystallinity in real time and the changes in morphology, for nanosecond and femtosecond pulse heating, two types of processes are identified: one that occurs at early time and involves a nondiffusive motion and another that takes place on a longer time scale. Similar mechanisms of two distinct time scales may perhaps be important in biomolecular folding, as suggested in ref 31.

3.5. Nanomechanical Phenomena. Uncovering the mechanisms of the function of nanoscale phenomena requires direct imaging at sufficiently high spatial and temporal resolutions. Equally importantly, such visualization provides understanding of the fundamental nature of the physical forces, which drive the directed function in these complex systems.

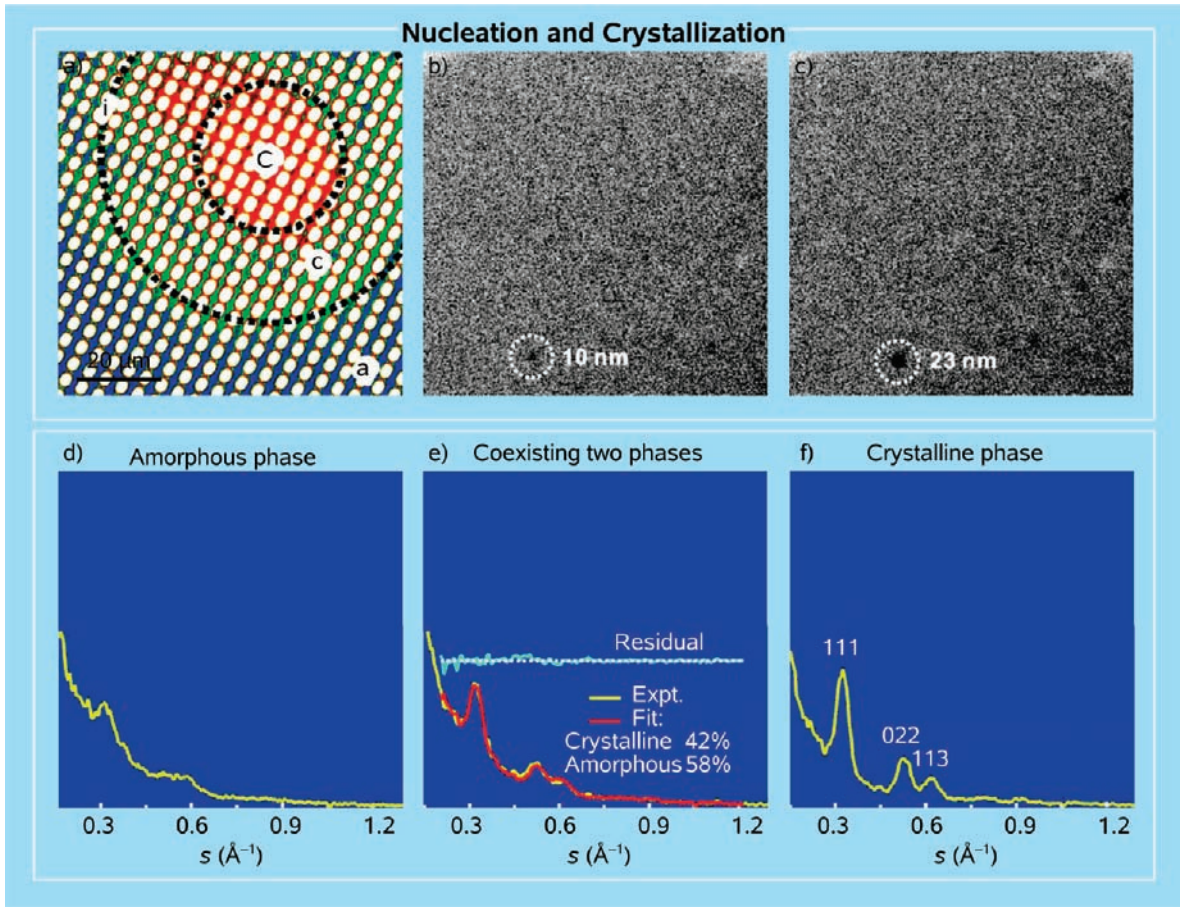

Figure 8. UEM imaging of nucleation and crystallization. (a) The response after a single laser-pulse heating. The zones are identified by circles to indicate the amorphous (a), the interfacial (i), and the two crystalline (c and C) phases. (b,c) The growth of crystallite size, with the transition from amorphous to polycrystalline state being evident in the images. Also shown are radially averaged diffraction patterns before (d), during (e), and after (f) the transformation, taken from the same sample area of irradiation. To fit a transient-frame diffraction profile (e), the negative-time (d) and asymptotic profiles (f) are combined in proportion of their contributions. For the quality of a fit, the difference between the transient-frame profile and the fitted one is also depicted. The high signal-to-noise ratio proved essential for the accuracy displayed.[31]

3.5.1. Channels Mechanics and Melting. The first of our examples comes from a study of transitions induced in a quasi-one-dimensional semiconductor, copper 7,7,8,8-tetracyanoquinodimethane (Cu-TCNQ), carried out using UEM-1. In micrometer-length crystals, the material exhibits a mechanical (nanoscale) molecular phenomenon, a switchable channel or *gate* (Figure 9).[33] The gate was controlled using the excitation shock induced in the sample by near-infrared laser pulses. The switching, after a shock, not only is temporally reversible when the pulses are on or off but also returns the material in real space to the original structure. The functional behavior is robust in the relatively low-fluence regime. Figure 9 shows a Cu-TCNQ single crystal that has been shocked by initially applying a burst of the laser light. Following this shock, the crystal was observed to fracture and separate by tens of nanometers depending upon the fluence of the initial pulse sequence. At significantly higher fluences, in the microscope, the internal dilation and the reduction of the copper ions were observed. This oxidation/reduction process is evident in the formation of islands of neutral copper metal structures identified from their diffraction patterns.

The mechanism derived from the microscopic images and diffraction patterns involves a nonthermal electron-transfer process. In single crystals of the Cu-TCNQ charge-transfer complex, Cu^+ and $TCNQ^-$ form discrete columnar stacks in a face-to-face configuration with strong overlap in the π-system. Further, the copper atoms are bound in a four-coordinate, highly distorted tetrahedral geometry to the nitrogen atoms on the cyano groups of the TCNQ moieties. The strong through-space interactions between the π-electrons result in quasi-1D structure of the material in the solid state. As seen in the crystal structure in Figure 9b, the *a*-axis is unique for stacking. Hence, the large anisotropy of gating must reflect the unique changes along the stacking axis [100] and not perpendicular to it. The modulation (i.e., closing and opening) of the channel is a modulation of the π-electron interactions of the stacked TCNQ molecules as a result of the charge transfer from $TCNQ^-$ to Cu^+, and elasticity of the material. This same reduction process is responsible for the formation of metallic copper islands; the fraction of complexes undergoing the electron transfer increases at higher fluences. The findings, especially at low fluences, may be of value in applications involving molecular nanoswitches and channels, as well as optical pulse memory.

3.5.2. Nanomechanics of Cantilevers. Another dimension to UEM is in the study of *in situ* structural transformations during a macroscopic function. The change is directly visualized in the variation of the properties of the material itself as it functions. As such, the properties can be used to discover and optimize nano(micro)electromechanical systems (NEMS and MEMS).[34] In principle, the use of optical methods (e.g., reflection/interferometry) can provide the ultrafast temporal resolution, but not the 3D spatial structure. On the other hand, conventional electron microscopy can image the structure in

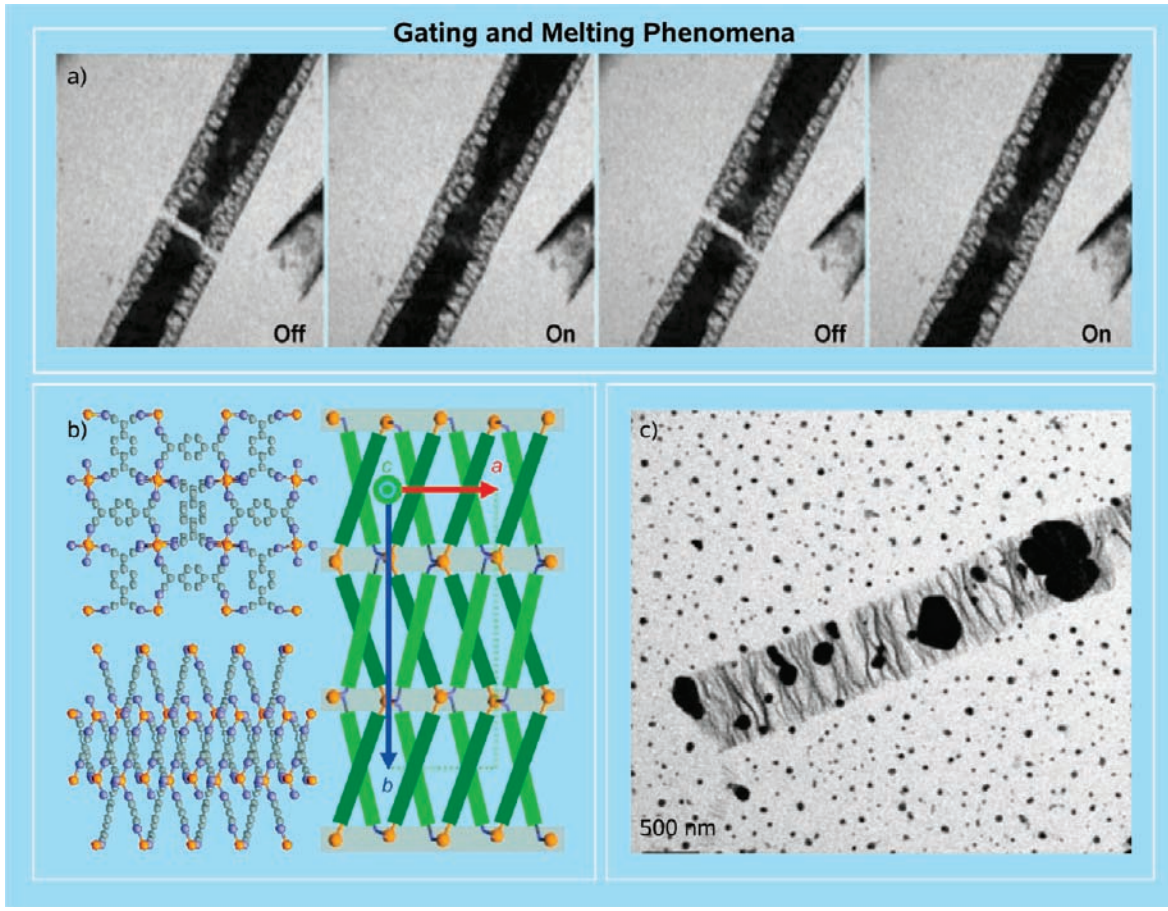

Figure 9. UEM images and crystal structure of Cu-TCNQ. Shown are micrographs taken in the already shocked single crystal of the material in the absence ("off") and in the presence ("on") of pulsed-laser irradiation (a). The channel width W varied from 0 (pulsed laser irradiation) to 140(5) nm (no pulsed-laser irradiation) over a series of 50 frames. Crystal structure of Cu-TCNQ and ultrafast melting of the material at high laser fluences are presented in panels (b) and (c), respectively.[33]

real space but has a temporal resolution of milliseconds, being limited by the frame rate of a CCD detector.

Direct visualization of nano- and microscale cantilevers and the (resonance) oscillations of their mechanical motions has recently been reported.[35] The static structures were constructed from a tomographic tilt series of images, whereas the *in situ* temporal evolution was determined using the stroboscopic configuration of UEM. Cu-TCNQ formed the nano- and microscale systems under study. The optomechanical motions are triggered by the charge transfer from the TCNQ radical anion ($TCNQ^-$) to copper (Cu^+), as discussed above. More than a thousand frames were recorded to provide a movie of the 3D movements of cantilevers in time. The expansions are colossal, reaching the micrometer scale, and the spatial modes were resolved on the nanoscale in the images (and angstrom-scale in diffraction) with resonances of megahertz frequencies for the fixed−free cantilevers. From these results, the Young's modulus, the force, and the energy stored in the cantilevers were obtained.

Tilt-series images obtained using UEM-1 provided the 3D coordinates of the cantilevers. The dimensions and protrusion angles of these free-standing crystals were characterized by taking static frames at different rotational angles of the substrate and made to construct the movie of their 2D projections. The 4D space−time evolution of cantilevers is shown in Figure 10a,b. The referenced (to negative time, $t_{ref} = -10$ ns; i.e., before the arrival of the clocking pulse) images of the microscale and nanoscale free-standing single crystal clearly display modes of expansion on the megahertz scale. Each image illustrates how the spatial location of the crystal has changed relative to the reference image as a function of the time delay, elucidating both the longitudinal and transverse displacements relative to the at-rest position. The displacements of the microscale cantilever as a function of time, in both the longitudinal and transverse directions, are displayed in Figure 10c, along with the digital Fourier transforms (FT) of the observed spatial oscillations for the time range shown (i.e., 0−3.3 μs). The motions in both directions of measurement are characterized by a large initial displacement from the at-rest position. The maximum longitudinal expansion possible (after accounting for the protrusion angle) for the 10 μm crystal is 720 nm, or over 7% of the total length!

Taking 3 MHz to be the main fundamental flexural frequency of the cantilever, one obtains Young's elastic modulus of the material, which was determined to be 2 GPa, with the speed of sound, therefore, being 1100 m/s. The potential energy stored and the force exerted at the moment of full extension along the long axis just after time zero were also estimated from the amplitudes and using Hooke's law. Values of 200 pJ and 600 μN were obtained for the potential energy and force, respectively, considering the maximum possible expansion of 720 nm;

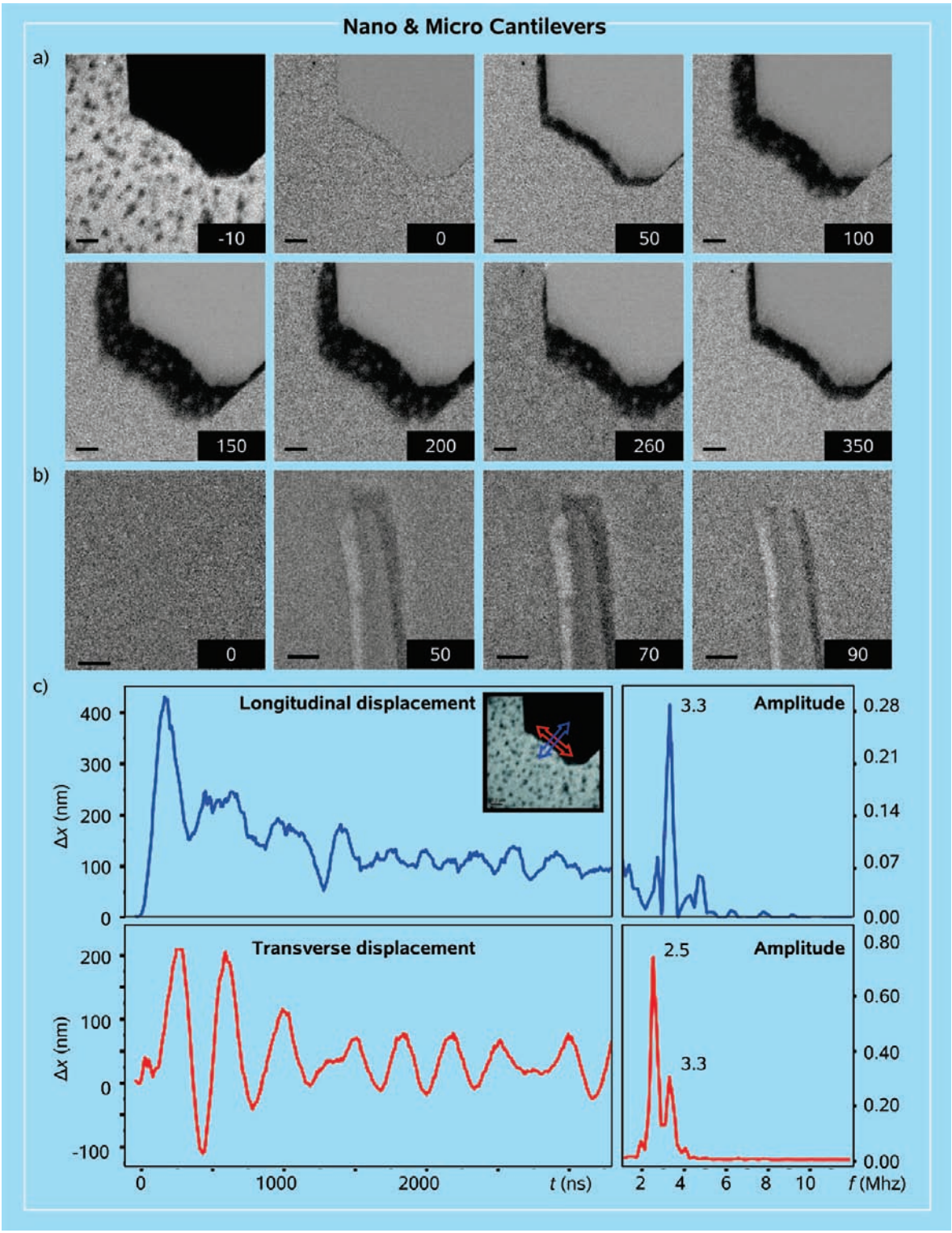

Figure 10. Mechanical resonances of cantilevers. Shown are 4D electron micrographs of the microscale (a) and nanoscale (b) Cu-TCNQ cantilevers. The frames recorded at positive times (nanoseconds) show referenced images with respect to the frame recorded at a negative time. The images illustrate the characteristic dynamics. Also shown are the initial displacements with subsequent oscillatory motions and frequencies of microscale Cu-TCNQ cantilevers (c). The longitudinal and transverse directions are defined as being parallel and perpendicular to the crystallographic *a* axis, respectively, and are illustrated by the blue (longitudinal) and red (transverse) directional arrows in the figure inset. All measured crystal positions are relative to the at-rest position at a negative time delay. The frequencies in the longitudinal and transverse directions (lower right) were obtained by FFT of the displacement responses (lower left).[35]

even when the amplitude is at its half value, the force is very large (~300 μN). In other words, because of molecular stacking, the force is very significant. Also, because of the microscale cross-section, the pressure of expansion translates to 0.1 GPa, only a few orders of magnitude less than the pressures exerted by a diamond anvil.

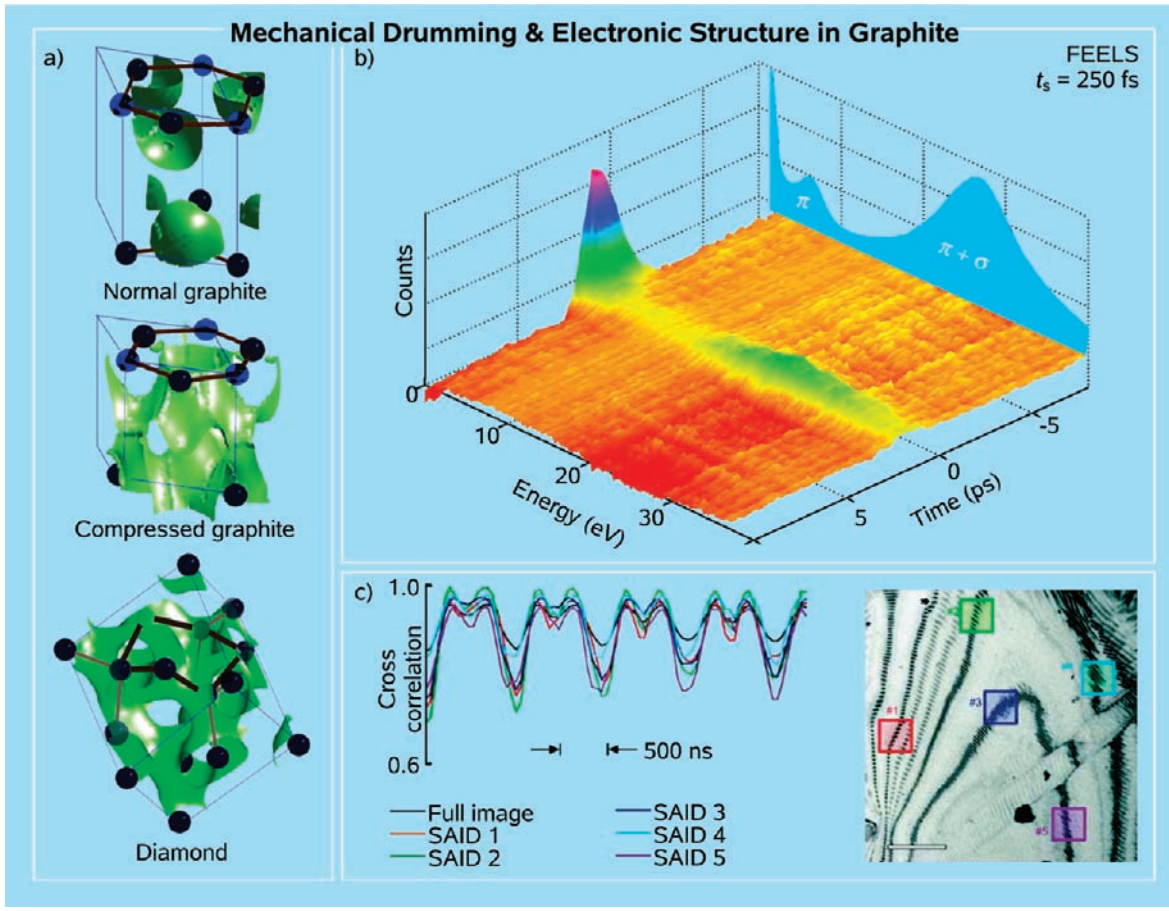

Figure 11. Mechanical resonance and electronic structure of graphite. Shown are envelope surfaces of constant electron density in normal graphite, compressed graphite, and diamond (a), femtosecond-resolved 3D time-energy-amplitude evolution of EEL spectra (FEELS) along with the EEL spectrum of graphite at negative times (b), and membrane-like drumming in a macroscopic film (c). Selected-area image dynamics of five different regions indicated in the micrograph reveals the evolution from the "chaotic" to the global resonance (drumming) behavior at long times.[36]

Knowing the dimensions of the material, and the laser fluence and absorptivity, the maximum pulse energy absorbed by the crystal is 30 nJ, and this means that, of the initial optical energy, a minimum of ~1% is converted into mechanical motion. In fact, it could reach 10% or more as determined by the projection of the electric field of light on the crystal. Similar results were obtained from the nanoscale cantilevers, and the resonance frequency scales correctly with the dimension. The observed function is robust, at least for 10^7 continuous pulse cycles (~10^{11} oscillations for the recorded frames), with no damage or plasticity.

4. Emerging Developments

Building on the concepts, techniques, and applications given above, further developments and applications can perhaps be defined by three major directions of research: materials science, biological imaging, and experimental (variant) techniques. Also of significance is the theoretical machinery needed for the determination of structural dynamics and for the visualization of complex systems.

In materials science, there are opportunities for the exploration of structural dynamics on different length and time scales and in different materials. A prime example of such evolutions in time and length scales is given by the UEM studies of 2D graphite. In this case, the phenomena involved vary from atomic motions at early time and short length scale to mechanical drumming at longer times and macroscopic length scales. Here, the available machinery of UEM and UEC were involved: diffraction, real-space imaging, and EELS (Figure 11).[12b,18,36] A comprehensive account of this line of research can be found in ref 9. Other examples of applications include the extension to studies of the phenomenon of diffusionless reactions in materials. It should also be possible to uncover new facts about the enigmatic catalytic activity of nanoparticle gold (supported on certain oxides).[9]

Biological imaging basically involves two approaches: electron crystallography, which relies on "redundancy" of the unit-cell repetition in crystals, and imaging of an ensemble of single (isolated) particles.[37] As mentioned above, so far, with cryo-UEM, stroboscopic images of the protein catalase crystals were obtained, resolving the 9.3-nm lattice planes, and bacterial cells (*Caulobacter crescentus*) displaying the membrane structure and flagellum were imaged (Figure 6). For the purpose of a single-pulse recording, the challenge is in ensuring that the lateral coherence is sufficient to see not only the object as a whole but also the structure within. Last, UEM opens up the possibility of recording femtosecond (or longer) time scale dynamics. It is conceivable to obtain time frames of single particles after an excitation pulse warms the sample, excites a conformational change, or releases a photocaged reactant. The regularity of pulsed dosing may result in the control of energy redistribution and heat dissipation, especially with substrates. These and other features are currently under investigation, and work is in progress to optimize the phase contrast of images.

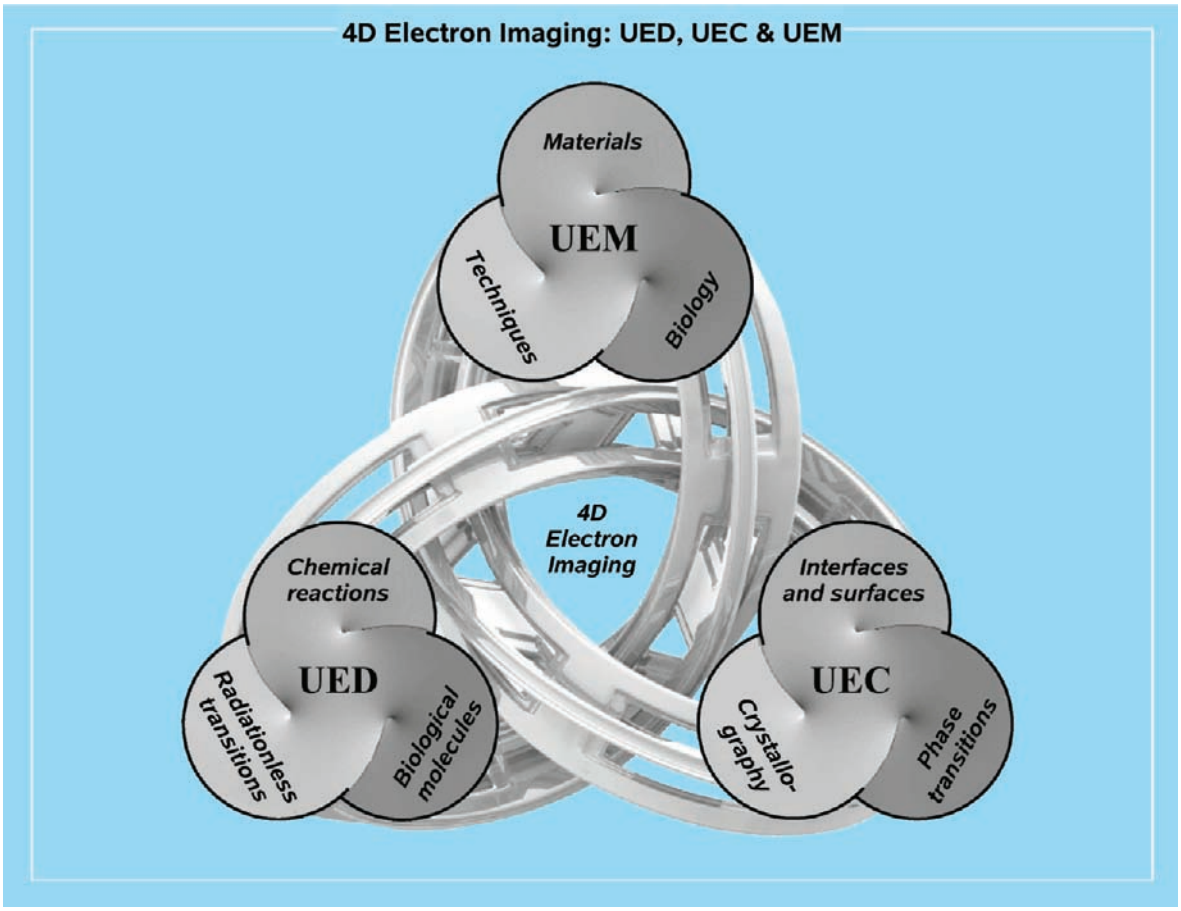

Figure 12. "Trefoil knot" of 4D electron imaging. Artistically represented is the interconnection between ultrafast electron microscopy (UEM), crystallography (UEC), and diffraction (UED).

On the theoretical front, with the increased complexity of systems studied, of prime significance is the development of the computational machinery required for the frame-by-frame deciphering of the ultrafast structural changes recorded in UED, UEC, and UEM experiments. Due to the complex nature of the ephemeral phenomena under study, experiment and theory often have to go hand-in-hand in unraveling details of the microscopic forces involved. For UED, there exist different algorithms that can be used to refine the structure for each particular point in time (temporal frame).[38] In imaging, millions of frames are involved in making movies of the actual, overall structural change. Similarly, for macromolecules there exist a myriad of conformations and populations. With the advent of such numerical experiments, the explicit dynamical trajectories of the "specimen" can be pictured with an atomic resolution, and the ensemble convergence can be achieved at increasingly longer time scales. Even in the case of a relatively small macromolecule, such as a DNA hairpin, the complexity of the energy landscape demands these new tools of computations.[39]

Of special interest to us are the manifestations of biological complexity in diffraction, first *in vacuo* and then after incorporation of the effect of hydration. Here again we embarked on both the analytical theoretical approach and the numerical experiments, especially when considering the myriad of structural configurations and the unique features of diffraction. This complexity could, naively, suggest the masking of any significant change in diffraction. However, an accurate theoretical mapping of order−disorder transitions in large molecular ensembles indicated that the problem of tracking down the disruption of the structural ordering in space and time may be experimentally tractable due to the unique coherence in scattering (*spatial resonance*) associated with the quasi-periodic secondary structure in the macromolecule.[40] Another example is that of DNA, which retains its major structural features even in the absence of the hydrating water layer.[41] Very recently, the structural dynamics of DNA unfolding *in vacuo*—as obtained from ensemble-convergent MD simulations carried out for a number of protonation states and temperature jumps—was reported along with a comparison of the unfolding dynamics of the same macromolecule in aqueous solution.[40a] Together with robust analytical models, such as the *kinetic intermediate structure* (KIS) model,[39] these capabilities provide the base for designing new experiments and testing concepts pertinent to complexity. At Caltech, a new UED instrument for this purpose is now operational.

On the technical side, the possibility of extending the temporal resolution to the sub-femtosecond domain was explored in a series of recent papers from this laboratory. Stimulated by developments in optical pulse generation,[42] novel methods have been suggested for achieving such pulses in electron imaging.[10,43] These methods could open the door for studies of electron dynamics on surfaces. In other developments, convergent-beam and near-field 4D electron microscopy methods were recently shown to map nanoscale structures and fields,[44] and EELS, which is now improved in time resolution by 10 orders of magnitude,[36a] can be extended to fundamental studies of electron densities.

5. Epilogue

Nobody would have anticipated the imaging capabilities that had emerged from J. J. Thomson's discovery of the electron in 1897 and L. de Broglie's particle-wave duality concept introduced in 1924—a lesson in the importance of curiosity-driven, fundamental research! The invention of the electron microscope in 1933 by M. Knoll and E. Ruska, together with many other advances, made possible the visualization of atoms, charge-density maps, complex materials, hydrated proteins, and single-particle ribosome structures, viruses, and cells. A recent monograph[9] gives a comprehensive overview of the major developments consequential upon the invention of the electron microscope. Our aim here is to emphasize the significance of the fourth (temporal) dimension when introduced in imaging of molecular and materials phenomena by electron microscopy, crystallography, and diffraction (Figure 12). The examples given above demonstrate the scope of applications and the emerging developments which, we hope, will stimulate research in many areas by utilizing the powerful arsenal of variant techniques of 4D electron imaging. The future should be as rich as the past, especially when considering molecular and materials complexity involving thousands and millions of atoms.

Acknowledgment. This research was carried out with the support from the National Science Foundation and Air Force Office of Scientific Research at the Physical Biology Center for Ultrafast Science and Technology (UST) established at Caltech by the Gordon and Betty Moore Foundation. We express our sincere gratitude to members of our laboratories, past and present, who contributed significantly to the research discussed here in UED, UEC and UEM; the names of those involved in the work reported here are given in the References section. This article builds on earlier reviews[13c,45] and, together with a recent monograph,[9] it provides an overview of the progress made so far.

References

(1) Zewail, A. H. *Annu. Rev. Phys. Chem.* **2006**, *57*, 65–103, and references therein.
(2) (a) Maxwell, L. R. *Phys. Rev.* **1933**, *44*, 73–76. (b) Lengyel, S.; Kalman, E. *Nature* **1974**, *248*, 405–406.
(3) Zewail, A. H. *Angew. Chem., Int. Ed.* **2000**, *39*, 2587–2631. Originally published in *Les Prix Nobel: The Nobel Prizes 1999*; Frängsmyr, T., Ed.; Almqvist & Wiksell: Stockholm, 2000; pp 110−203.
(4) Polanyi, J. C.; Zewail, A. H. *Acc. Chem. Res.* **1995**, *28*, 119–132.
(5) (a) Thomas, J. M. In *Physical Biology: From Atoms to Medicine*; Zewail, A. H., Ed.; Imperical College Press: London, 2008; pp 51−114. (b) Thomas, J. M. *Angew. Chem., Int. Ed.* **2005**, *44*, 5563–5566. (c) Harris, K. D. M.; Thomas, J. M. *Cryst. Growth Des.* **2005**, *5*, 2124–2130. (d) Thomas, J. M. *Angew. Chem., Int. Ed.* **2004**, *43*, 2606–2610. (e) Thomas, J. M. *Nature* **1991**, *351*, 694–695.
(6) (a) Chergui, M.; Zewail, A. H. *Chem. Phys. Chem.* **2009**, *10*, 28–43. (b) Bressler, C.; Chergui, M. *Chem. Rev.* **2004**, *104*, 1781–1812, and references therein.
(7) Baskin, J. S.; Zewail, A. H. *J. Chem. Educ.* **2001**, *78*, 737–751.
(8) (a) Zewail, A. H. *Nature* **2001**, *412*, 279. (b) Zewail, A. H. *Angew. Chem., Int. Ed.* **2001**, *40*, 4371–4375.
(9) Zewail, A. H.; Thomas, J. M. *4D Electron Microscopy: Imaging in Space and Time*; Imperial College Press: London, 2009, and references therein.
(10) Baum, P.; Zewail, A. H. *Proc. Natl. Acad. Sci. U.S.A.* **2007**, *104*, 18409–18414.
(11) Zewail, A. H.; Lobastov, V. A. U.S. Patent 7 154 091, 2006.
(12) (a) Park, H. S.; Baskin, J. S.; Kwon, O.-H.; Zewail, A. H. *Nano Lett.* **2007**, *7*, 2545–2551. (b) Barwick, B.; Park, H. S.; Kwon, O.-H.; Baskin, J. S.; Zewail, A. H. *Science* **2008**, *322*, 1227–1231.
(13) (a) Ihee, H.; Lobastov, V. A.; Gomez, U. M.; Goodson, B. M.; Srinivasan, R.; Ruan, C.-Y.; Zewail, A. H. *Science* **2001**, *291*, 458–462. (b) Srinivasan, R.; Feenstra, J. S.; Park, S. T.; Xu, S.; Zewail, A. H. *Science* **2005**, *307*, 558–563. (c) For a comprehensive review of early work, see: Srinivasan, R.; Lobastov, V. A.; Ruan, C.-Y.; Zewail, A. H. *Helv. Chim. Acta* **2003**, *86*, 1763–1838. Examples of X-ray scattering studies in solution: (d) Lee, J. H.; Kim, T. K.; Kim, J.; Kong, Q.; Cammarata, M.; Lorenc, M.; Wulff, M.; Ihee, H. *J. Am. Chem. Soc.* **2008**, *130*, 5834–5835. (e) Ihee, H.; Lorenc, M.; Kim, T. K.; Kong, Q. Y.; Cammarata, M.; Lee, J. H.; Bratos, S.; Wulff, M. *Science* **2005**, *309*, 1223–1227. See also: (f) Anfinrud, P.; Schotte, F. *Science* **2005**, *309*, 1192–1193.
(14) Zhong, D.; Ahmad, S.; Zewail, A. H. *J. Am. Chem. Soc.* **1997**, *119*, 5978–5979.
(15) Ihee, H.; Kua, J.; Goddard, W. A., III; Zewail, A. H. *J. Phys. Chem. A* **2001**, *105*, 3623–3632.
(16) (a) Ruan, C.-Y.; Lobastov, V. A.; Vigliotti, F.; Chen, S.; Zewail, A. H. *Science* **2004**, *304*, 80–84. (b) Yang, D.-S.; Zewail, A. H. *Proc. Natl. Acad. Sci. U.S.A.* **2009**, *106*, 4122–4126.
(17) Andreussi, O.; Donadio, D.; Parrinello, M.; Zewail, A. H. *Chem. Phys. Lett.* **2006**, *426*, 115–119.
(18) Carbone, F.; Baum, P.; Rudolf, P.; Zewail, A. H. *Phys. Rev. Lett.* **2008**, *100*, 035501.
(19) Kubota, J.; Wada, A.; Kano, S. S.; Domen, K. *Chem. Phys. Lett.* **2003**, *377*, 217–222.
(20) (a) Chen, S.; Seidel, M. T.; Zewail, A. H. *Proc. Natl. Acad. Sci. U.S.A.* **2005**, *102*, 8854–8859. (b) Seidel, M. T.; Chen, S.; Zewail, A. H. *J. Phys. Chem. C* **2007**, *111*, 4920–4938. (c) Chen, S.; Seidel, M. T.; Zewail, A. H. *Angew. Chem., Int. Ed.* **2006**, *45*, 5154–5158.
(21) (a) Tang, J.; Yang, D.-S.; Zewail, A. H. *J. Phys. Chem. C* **2007**, *111*, 8957–8970. See also: (b) Tang, J. *J. Chem. Phys.* **2008**, *128*, 164702. Erratum: (c) Tang, J. *J. Chem. Phys.* **2008**, *129*, 179901.
(22) Wang, Z.; Carter, J. A.; Lagutchev, A.; Koh, Y. K.; Seong, N.-H.; Cahill, D. G.; Dlott, D. D. *Science* **2007**, *317*, 787–790.
(23) Ruan, C.-Y.; Yang, D.-S.; Zewail, A. H. *J. Am. Chem. Soc.* **2004**, *126*, 12797–12799.
(24) Lobastov, V. A.; Srinivasan, R.; Zewail, A. H. *Proc. Natl. Acad. Sci. U.S.A.* **2005**, *102*, 7069–7073.
(25) Edwards, P. P.; Johnston, R. L.; Rao, C. N. R.; Tunstall, D. P.; Hensel, F. *Phil. Trans. R. Soc. Lond. A* **1998**, *356*, 5–22, and references therein.
(26) Grinolds, M. S.; Lobastov, V. A.; Weissenrieder, J.; Zewail, A. H. *Proc. Natl. Acad. Sci. U.S.A.* **2006**, *103*, 18427–18431.
(27) Lobastov, V. A.; Weissenrieder, J.; Tang, J.; Zewail, A. H. *Nano Lett.* **2007**, *7*, 2552–2558.
(28) (a) Baum, P.; Yang, D.-S.; Zewail, A. H. *Science* **2007**, *318*, 788–792. (b) Cavalleri, A. *Science* **2007**, *318*, 755–756.
(29) Gedik, N.; Yang, D.-S.; Logvenov, G.; Bozovic, I.; Zewail, A. H. *Science* **2007**, *316*, 425–429.
(30) (a) Carbone, F.; Yang, D.-S.; Giannini, E.; Zewail, A. H. *Proc. Natl. Acad. Sci. U.S.A.* **2008**, *105*, 20161–20166. (b) Chen, Y. L.; Lee, W. S.; Shen, Z. X. *Proc. Natl. Acad. Sci. U.S.A.* **2009**, *106*, 963–964.
(31) Kwon, O.-H.; Barwick, B.; Park, H. S.; Baskin, J. S.; Zewail, A. H. *Proc. Natl. Acad. Sci. U.S.A.* **2008**, *105*, 8519–8524.
(32) Ruan, C.-Y.; Vigliotti, F.; Lobastov, V. A.; Chen, S.; Zewail, A. H. *Proc. Natl. Acad. Sci. U.S.A.* **2004**, *101*, 1123–1128.
(33) Flannigan, D. J.; Lobastov, V. A.; Zewail, A. H. *Angew. Chem., Int. Ed.* **2007**, *46*, 9206–9210.
(34) (a) Craighead, H. G. *Science* **2000**, *290*, 1532–1535. (b) Ekinci, K. L.; Roukes, M. L. *Rev. Sci. Instrum.* **2005**, *76*, 061101.
(35) Flannigan, D. J.; Samartzis, P. C.; Yurtsever, A.; Zewail, A. H. *Nano Lett.* **2009**, *9*, 875–881.
(36) (a) Carbone, F.; Kwon, O.-H.; Zewail, A. H. *Science* **2009**, *325*, 181–184. (b) Carbone, F.; Barwick, B.; Kwon, O.-H.; Park, H. S.; Baskin, J. S.; Zewail, A. H. *Chem. Phys. Lett.* **2009**, *468*, 107–111. (c) Kwon, O.-H.; Barwick, B.; Park, H. S.; Baskin, J. S.; Zewail, A. H. *Nano Lett.* **2008**, *8*, 3557–3562.
(37) (a) Glaeser, R. M.; Downing, K.; DeRosier, D.; Chiu, W.; Frank, J. *Electron Crystallography of Biological Macromolecules*; Oxford University Press: New York, 2007. (b) Frank, J. *Three-Dimensional Electron Microscopy of Macromolecular Assemblies: Visualization of Biological Molecules in their Native State*; Oxford University Press: New York, 2006.
(38) (a) Shorokhov, D.; Park, S. T.; Zewail, A. H. *Chem. Phys. Chem.* **2005**, *6*, 2228–2250. (b) Habershon, S.; Zewail, A. H. *Chem. Phys. Chem.* **2006**, *7*, 353–362. (c) Ruan, C.-Y.; Lobastov, V. A.; Srinivasan, R.; Goodson, B. M.; Ihee, H.; Zewail, A. H. *Proc. Natl. Acad. Sci. U.S.A.* **2001**, *98*, 7117–7122.
(39) Lin, M. M.; Meinhold, L.; Shorokhov, D.; Zewail, A. H. *Phys. Chem. Chem. Phys.* **2008**, *10*, 4227–4239.
(40) (a) Lin, M. M.; Shorokhov, D.; Zewail, A. H. *Phys. Chem. Chem. Phys.* **2009**, *11*, 10619−10632. (b) Lin, M. M.; Shorokhov, D.; Zewail, A. H. *J. Phys. Chem. A* **2009**, *113*, 4075–4093. (c) Lin, M. M.; Shorokhov, D.; Zewail, A. H. *Chem. Phys. Lett.* **2006**, *420*, 1–7.

(41) See, for example: Rueda, M.; Kalko, S. G.; Luque, F. J.; Orozco, M. *J. Am. Chem. Soc.* **2003**, *125*, 8007–8014, and references therein.
(42) Krausz, F.; Ivanov, M. *Rev. Mod. Phys.* **2009**, *81*, 163–234, and references therein.
(43) (a) Hilbert, S. A.; Uiterwaal, C.; Barwick, B.; Batelaan, H.; Zewail, A. H. *Proc. Natl. Acad. Sci. U.S.A.* **2009**, *106*, 10558–10563. (b) Baum, P.; Zewail, A. H. *Chem. Phys.*, doi: 10.1016/j.chemphys.2009.07.013. (c) Baum, P.; Zewail, A. H. *Chem. Phys. Lett.* **2008**, *462*, 14–17. (d) Baum, P.; Zewail, A. H. *Proc. Natl. Acad. Sci. U.S.A.* **2006**, *103*, 16105–16110.
(44) (a) Yurtsever, A.; Zewail, A. H. *Science* **2009**, *326*, 708−712. (b) Barwick, B.; Flannigan, D. J.; Zewail, A. H. *Nature*, in press.
(45) Shorokhov, D.; Zewail, A. H. *Phys. Chem. Chem. Phys.* **2008**, *10*, 2879–2893.
(46) (a) Feenstra, J. S.; Park, S. T.; Zewail, A. H. *J. Chem. Phys.* **2005**, *123*, 221104. (b) Park, S. T.; Feenstra, J. S.; Zewail, A. H. *J. Chem. Phys.* **2006**, *124*, 174707.
(47) He, Y.; Gahlmann, A.; Feenstra, J. S.; Park, S. T.; Zewail, A. H. *Chem.-Asian J.* **2006**, *1*−*2*, 56–63.
(48) Park, S. T.; Gahlmann, A.; He, Y.; Feenstra, J. S.; Zewail, A. H. *Angew. Chem., Int. Ed.* **2008**, *47*, 9496–9499.
(49) Gahlmann, A.; Park, S. T.; Zewail, A. H. *J. Am. Chem. Soc.* **2009**, *131*, 2806–2808.
(50) (a) Srinivasan, R.; Feenstra, J. S.; Park, S. T.; Xu, S.; Zewail, A. H. *J. Am. Chem. Soc.* **2004**, *126*, 2266–2267. (b) Xu, S.; Park, S. T.; Feenstra, J. S.; Srinivasan, R.; Zewail, A. H. *J. Phys. Chem. A* **2004**, *108*, 6650–6655.

JA907432P